ADSORPTION AND GROWTH ON Si(001) SURFACE

A THESIS SUBMITTED TO
THE GRADUATE SCHOOL OF NATURAL AND APPLIED SCIENCES
OF
THE MIDDLE EAST TECHNICAL UNIVERSITY

BY

RIAD SHALTAF

IN PARTIAL FULFILLMENT OF THE REQUIREMENTS FOR THE DEGREE OF

DOCTOR OF PHILOSOPHY

IN

THE DEPARTMENT OF PHYSICS

APRIL 2004

Approval of the Graduate School of Natural and Applied Sciences.

_____

Prof. Dr. Canan Özgen
Director

I certify that this thesis satisfies all the requirements as a thesis for the degree of Doctor of Philosophy.

_____

Prof. Dr. Sinan Bilikmen
Head of Department

This is to certify that we have read this thesis and that in our opinion it is fully adequate, in scope and quality, as a thesis for the degree of Doctor of Philosophy.

_____

Prof. Dr. Şinasi Ellialtıoğlu
Supervisor

Examining Committee Members

Prof. Dr. Cemal Yalabık   _____

Prof. Dr. Şinasi Ellialtıoğlu   _____

Prof. Dr. Bülent Akınoğlu   _____

Prof. Dr. Şenay Katırcıoğlu   _____

Instr. Dr. Sadi Turgut   _____

ABSTRACT

ADSORPTION AND GROWTH ON Si(001) SURFACE

Shaltaf, Riad

Ph. D., Department of Physics

Supervisor: Prof. Dr. Şinasi Ellialtıoğlu

April 2004, 108 pages

The (001) surface of silicon has been the topic of our study in this thesis. The clean surface, an-adatom or submonolayer adsorption on the surface, the monolayer adsorption and its stability conditions as well as growth simulation on the surface were investigated using the state of the art techniques.

We have used *ab initio* density functional calculations based on norm-conserving pseudopotentials to investigate the Mg adsorption on the Si(001) surface for 1/4, 1/2 and 1 monolayer (ML) coverages. For both 1/4 and 1/2 ML coverages it has been found that the most favorable site for the Mg adsorption is the cave site between two dimer rows consistent with recent experiments. For the 1 ML

coverage (2 Mg atoms per 2× 1 unit cell)we have found that the most preferable configuration is when both Mg atoms on 2×1 reconstruction occupy the two shallow sites. We have found that the minimum energy configurations for 1/4 ML coverage is a 2×2 reconstruction while for the 1/2 and 1 ML coverages they are 2×1.

Same method was also used to investigate the surface stress and energetics of the clean-, Sb-adsorbed-, and Sb-interdiffused-Si(001) surface. It is found that interdiffusion of Sb into deeper layers of Si(001) leads to a more isotropic surface stress but corresponds to a higher total energy configuration. As a result of competition between stress relief and energy gain, the surface with all the Sb atoms adsorbed on top of Si(001) surface layer is predicted to have a less ordered geometry and roughness in z-direction. We have repeated the similar calculations on the Ge(001) surface for comparison.

Finally using empirical molecular dynamics method, we have investigated the crystalline growth of silicon on Si(001) as a function of substrate temperature and incident particle energy. Our results show that the increase of substrate temperature enhances the crystallinity in the film grown on the Si(001) surface, on the other hand, the crystalline growth can be enhanced at low temperature by using higher incidence energy.

Keywords: Silicon, Germanium, Magnesium, Antimony, adsorption, energy bands, crystal growth, ab-initio, first-principles, molecular dynamics simulation, Stillinger-Weber potential

ÖZ

Si(001) YÜZEYINDE TUTUNMA VE BÜYÜME

Shaltaf, Riad

Doktora, Fizik Bölümü

Tez Yöneticisi: Prof. Dr. Şinasi Ellialtıoğlu

Nisan 2004, 108 sayfa

Bu tezde çalışma konumuzu silicon (001) yüzeyi oluşturmuştur. Temiz yüzey, yüzeyde ek-atom veya katman-altı ve tek-katman eklenmesi, tek-katman kaplı yüzeyde kararlılık koşulları ile yüzeyde kristal büyütmenin bezetişimi en son yöntemler kullanılarak incelenmiştir. Si(001) yüzeyinde 1/4, 1/2 ve 1 katmanlık Mg tutunmasını incelemek için norm-koruyan potansiyelimsilere dayanan ilk-ilke yoğunluk fonksiyonel hesapları yapılmıştır. Bunlardan 1/4 ve 1/2 katmanlı kaplamaların herikisi için de Mg atomunun tutunduğu en öncelikli yerin dimer-sıraları arasında bulunan "mağara" tipi konum olduğu deneylerle de uyumlu olarak bulunmuştur. Tek-katman kaplandığında (2×1 birim hücre içinde 2 Mg atomu) en

çok tercih edilen yerleşim biçiminin, heriki Mg atomunun da 2×1 yapılanmasında bulunan iki "sığ" konumu işgal etmeleri ile elde edildiği görülmüştür. En düşük enerji konfigürasyonları olarak 1/4 katmanlı kaplamada 2×2 yapılanması, 1/2 ve 1 katmanlı kaplamalarda ise 2×1 yapılanması bulunmuştur.

Aynı yöntem, temiz-, Sb-tutunmuş-, ve Sb-nüfuz etmiş Si(001) yüzeylerinin enerjetik ve yüzey stres yapısının incelenmesinde kullanılmıştır. Sb'un Si(001) yüzeyinden daha derin katmanlara nüfuz etmesi sonucu yüzey stresinin daha izotropikleştiği ancak daha yüksek toplam enerjiye ulaşıldığı görülmüştür. Stres boşalması ve enerji artımı arasındaki rekabetin sonucunda tüm Sb atomlarının Si(001) yüzey katmanı üzerinde tutundukları böyle bir yüzeyin az-düzenli bir geometriye ve z-yönünde bir pürüzlülüğe sahip olması öngörülmektedir. Karşılaştırma yapmak gayesiyle Ge(001) yüzeyi için de benzer hesaplar tekrarlanmıştır.

Son olarak ampirik moleküler dinamik yöntemi kullanılarak Si(001) alttaşı üzerine silikon büyütülmesi, alttaş sıcaklığı ve atomların geliş enerjisi cinsinden incelenmiştir. Sonuçlar, büyütülen filmin billurluğunun alttaş sıcaklığı ile, ve diğer taraftan, düşük sıcaklıkta ise yüksek geliş enerjisi ile arttığını göstermiştir.

Anahtar Kelimeler: Silikon, Germanyum, Magnesyum, Antimon, Yüzerme, enerji bandı, kristal büyütme, ab-initio, ilk-ilke, moleküler dinamik benzetişimi, Stillinger-Weber potansiyeli

To My Parents

ACKNOWLEDGMENTS

TABLE OF CONTENTS

x

LIST OF TABLES

LIST OF FIGURES

CHAPTER I

INTRODUCTION

Semiconducting bulk materials have been the subject of extensive investigations, both experimentally and theoretically, for many decades. The reason behind this was the interesting electronic and optical properties exhibited by semiconductors. Since, however, the surfaces and interfaces of semiconductor materials play the main role in technology and device applications, most of the scientific interest was later directed to surface studies leading to what is known as surface science. For the past three decades there has been a momentous growth of research on semiconductor surfaces and interfaces, and related low-dimensional structures such as quantum wells, quantum wires and quantum dots.

Various experimental techniques are used to study the surfaces. Low energy electron diffraction (LEED), reflection high energy electron diffraction (RHEED), and scanning tunnelling microscopy (STM) are some of the typical experimental techniques that are used to determine the size and shape of surface unit cells and

1

hence the surface reconstruction. The electronic properties of surfaces can be studied using photoelectron spectroscopy (PS) which comes in different energy ranges as ultra violet photo electron spectroscopy (UPS) and X-ray photoelectron spectroscopy (XPS), the latter being more suitable for bulk studies. Angle resolved ultra violet photo electron spectroscopy (ARUPS) can be used to investigate dispersion of energy bands. Auger electron spectroscopy (AES) is another surface sensitive analytical technique that can be used to extract chemical information about surfaces.

On the other hand computational methods can be used to achieve the same goal, and in many times they are used hand in hand with experimental techniques to get a clear picture of physical phenomena under consideration. Since the aim of these computational methods will be always to calculate the total energy of some system under some specific conditions, the way this total energy is calculated will characterize the method. The methods that use quantum mechanical approach starting from the first principles in evaluating the total energy are called *ab initio* methods, examples of these methods are Hatree-Fock and density functional calculations. The importance of these methods exist in the fact that they are self starting with almost no approximations, the accuracy is good and most of the time they are in good agreement with the experimental results. But the drawback of these methods is that they are very expensive in memory requirement and CPU time which makes it very difficult to study systems with very large unit cells.

Another approach of calculating energy can be achieved by using empirical

potential energy functions (PEF). These functions are simple analytical expressions. They are usually written as functions of atomic coordinates and contain parameters fitted to experimental data or *ab initio* database. PEF can be in the form of two body, three body or even many body interactions. These functions are expected to have all the electronic effects implicitly contained in their formulation. Using PEF one can study large systems containing millions of atoms. But they are less reliable and may fail to replicate experimental results, since PEF are usually parameterized to fit some specific phase, and it may not be successful in describing other phases. Whatever was the method used in the calculation, the system can evolve in time or is driven to its minimum-energy-configuration by using a geometry optimization method. Molecular dynamics and Monte Carlo methods are two good examples universally used to achieve this goal.

Being the prototype material in semiconducting technology, silicon surfaces has been the subject of most of the experimental and theoretical studies using the above techniques. Silicon surfaces can be prepared by cleaving from a simple crystal or artificially growing on substrates with desired orientation using molecular beam epitaxy or ion bombardment in the laboratory. Si(001) having two dangling bonds per surface atom attracted more attention than low-index surfaces because of its importance in device technology and its reconstruction simplicity.

When the silicon (001) surface is prepared, atoms on the surface will have different environment than those inside the bulk. This difference is characterized by the existence of two dangling bonds for each surface atom. In order to minimize

3

Figure I.1: Different Si(001) reconstructions, top one is symmetric (2×1) , middle one is asymmetric (2×1) , below one is $p(2\times2)$ reconstruction.

the surface energy and the number of dangling bonds, the silicon surface atoms may deviate from their ideal bulk positions to new equilibrium positions leading to what is known as surface reconstruction. The first experimental suggestion for Si(001) reconstruction came from LEED experiment. It was argued that each two adjacent surface atoms will form a dimer saturating one of the two dangling bonds per surface atom, so it forms a 2×1 reconstruction [1]. The idea of dimerization as a basic machinery of reconstruction was used successfully in interpreting many other experimental results but unfortunately it has been shown that this leads to a metallic surface states in contradiction with the experimental results [2].

In order to solve this discrepancy between theory and experiment, Chadi [3] proposed an asymmetric dimer model in which atoms do not have the same height above the surface (asymmetric dimers). It was suggested that this buckling comes out as a result of charge transfer between the dimer atoms. Tight binding calculations showed that this surface model is semiconducting. The model of asymmetric dimers has been verified by many other experimental and theoretical studies, and it is found that it is lower in energy than that of the symmetric one. Other types of reconstructions, which have even lower energies than that of asymmetric (2×1) one, namely $p(2 \times 2)$ and $c(4 \times 2)$ have been observed at low temperatures using STM [4, 5], LEED [6], and ARUPS [7]. The *ab initio* and tight binding methods were successful in providing theoretical evidence for dimer tilting on Si(001) surfaces. However, methods that are based on empirical potential functions (PEF) were not. The reason behind this is the failure of empirical potentials in accounting for the charge transfer between the dimer atoms.

5

In Figure I.1 we show our theoretical results for Si(001) reconstruction. The symmetric dimer reconstruction was calculated using Stillinger-Weber potential [8] while (2×1) asymmetric and $p(2 \times 2)$ results are obtained by *ab initio* calculations. The surface energy bands associated with the symmetric and asymmetric dimers for (2×1) reconstructions are shown in Figure I.2 together with the bulk energy bands projected on the two dimensions as calculated using *ab initio* method.

The existence of dangling bonds on the surface is not preferable for technological purposes, since they are a source of surface states and the surface will be chemically reactive. The surface reconstruction naturally can eliminate some of these dangling bonds via dimerization. As stated before, the number of dangling bonds on Si(001) was decreased from two to one dangling bond per surface atom. For technological purposes, the remaining dangling bonds can be saturated with the adsorption of other elements. This makes it important to investigate the structural and electronic properties of these surfaces in the presence of adsorbed atoms. As the evaporated atoms get adsorbed on the growth surface in a crystal growth process, these atoms will start to migrate on the surface until they occupy a site that minimizes the surface energy. As a result, the surface will have different structural and consequently different electronic properties than those of the clean surface. It is important to note here that the structural and electronic properties of surfaces will change as the population of adsorbent atoms is increased and the adsorbent-adsorbent interaction becomes effective. This leads to the need of investigating these properties as a function of adsorbent coverage.
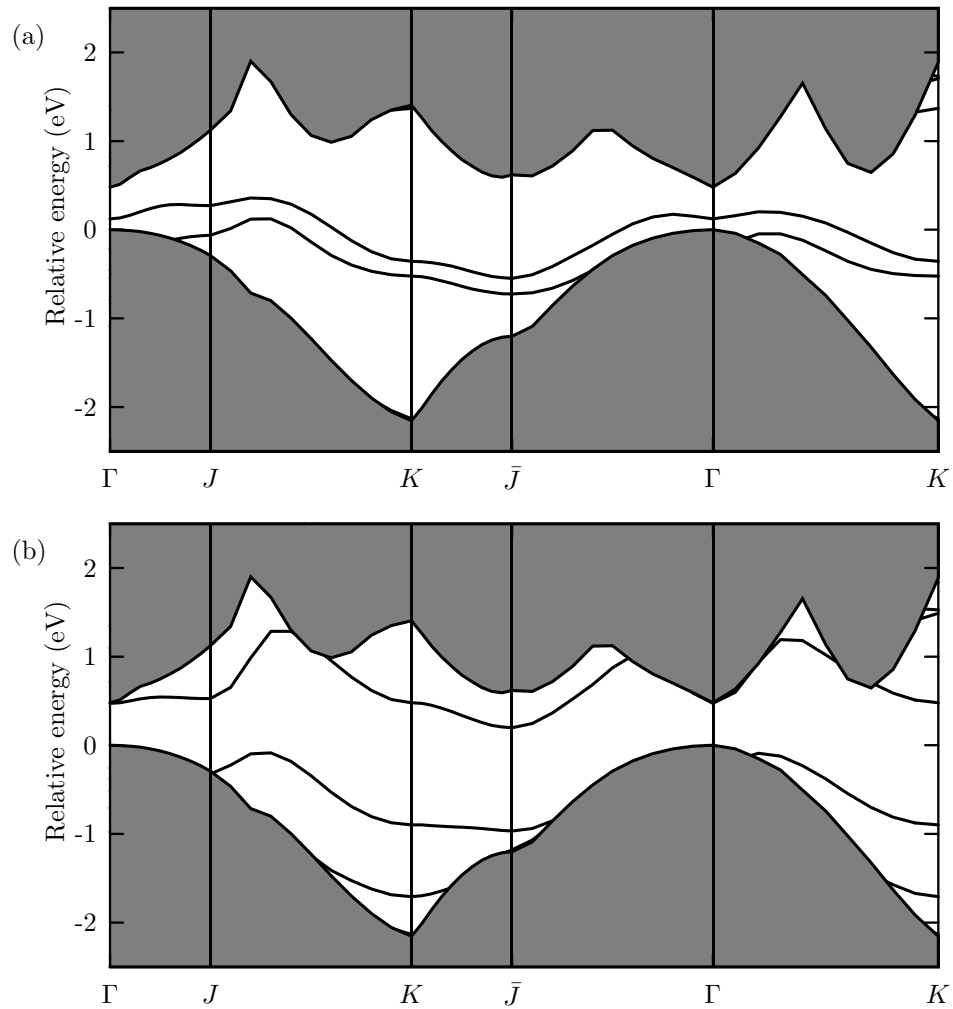
Figure I.2: Electronic band structure of the Si(001) 2x1 surface. (a) symmetric dimers (b) asymmetric dimers model. Projected bulk spectrum is shown by shaded region.

As the full coverage is reached how well the surface order is achieved becomes of interest since they effect the device quality. Surface stress may play a crucial rule in causing roughness and the formation of anti-domain phases on the surface, which are typical deviations from the surface order.

In real growth experiments, parameters like substrate temperature play a major rule. These experiments may also involve sending atoms to the surface with certain initial kinetic energies and allowing for some length of time interval for relaxation. Problems of this type are not yet conceivable to be handled with *ab initio* methods, but they can be studied using empirical PEF's.

In the second chapter, we will discuss briefly the theoretical methods used in this thesis. In the third chapter, we will use *ab initio* density functional theory to investigate the adsorption of Mg atoms on Si(001) for submonolayer and monolayer coverages. Chapter four presents the investigation of the stability of flat monolayer of Sb on Si(001) and Ge(001). In the fifth chapter we will investigate theoretically Si(001) crystal growth in a manner similar to what is done in the laboratory. We will check, using molecular dynamics simulations with empirical potentials, some of experimental parameters that affect the quality of grown Si(001). We will investigate the quality of crystalline material as a function of substrate temperature and incident particle energy.

CHAPTER II

THEORETICAL METHODS

II.1 *Ab initio* **Methods**

The ultimate goal of most quantum chemical approaches is the approximate solution of the time-independent, non-relativistic Schrödinger equation

$$\hat{H}\psi(\mathbf{r}_1, \mathbf{r}_2, ..., \mathbf{r}_n, \mathbf{R}_1, \mathbf{R}_2, ..., \mathbf{R}_m) = E\psi(\mathbf{r}_1, \mathbf{r}_2, ..., \mathbf{r}_n, \mathbf{R}_1, \mathbf{R}_2, ..., \mathbf{R}_m), \quad \text{(II.1)}$$

where $\hat{H}$ is the total energy operator for a molecular system consisting of m atoms and n electrons and given explicitly in reduced units

$$\hat{H} = \frac{1}{2}\sum_i^n \nabla_i^2 + \frac{1}{2M}\sum_j^m \nabla_j^2 + \frac{1}{2}\sum_i^n \sum_{j\neq i}^n \frac{1}{|\mathbf{r}_i - \mathbf{r}_j|} + \sum_i^n \sum_j^m \frac{Z_j}{|\mathbf{r}_i - \mathbf{R}_j|}$$
$$+ \frac{1}{2}\sum_i^m \sum_{j\neq i}^m \frac{Z_i Z_j}{|\mathbf{R}_i - \mathbf{R}_j|} \quad \text{(II.2)}$$

Because of the large difference in mass between the electrons and the nuclei and the fact that the forces on the particles are the same, the electrons respond instantly to the motion of the nuclei. Thus the nuclei can be treated adiabatically,

leading to a separation of the electronic and nuclear coordinates in the many body wave function. This is known as "Born-Oppenheimer approximation" [9]. In this case the Hamiltonian above reduces to an all electronic Hamiltonian:

$$
\begin{aligned}
\hat{H}^{\mathrm{el}} &= \frac{1}{2}\sum_i^n \nabla_i^2 + \frac{1}{2}\sum_i^n \sum_{j\neq i}^n \frac{1}{|\mathbf{r}_i - \mathbf{r}_j|} + \sum_i^n \sum_j^m \frac{Z_j}{|\mathbf{r}_i - \mathbf{R}_j|} \\
&= \hat{T}^{\mathrm{el}} + \hat{V}^{\mathrm{el-el}} + \hat{V}^{\mathrm{el-ion}}.
\end{aligned}
\tag{II.3}
$$

In principle it is impossible to solve Equation (II.3) considering the large number of electrons that exist in a solid. Further approximations must be made in order to find a manageable many body wave function and the total energy of the solid, which is our main goal.

II.1.1 Hartree and Hartree-Fock Approximations

In Hartree approximation [10], the many body wave function is approximated as a product of N single electron wave functions, i.e,

$$
\psi(\mathbf{r}_1, \mathbf{r}_2, ..., \mathbf{r}_n) = \prod_i \phi_i(\mathbf{r}_i).
\tag{II.4}
$$

If we take the expectation value of $\hat{H}$ using this type of many body wave function, we get

$$
\langle H \rangle = \sum_i \int d\mathbf{r}\,\phi_i^*(\mathbf{r})\left(-\frac{\nabla^2}{2} + V^{\mathrm{ion}}\right)\phi_i(\mathbf{r}) + \frac{1}{2}\sum_i \sum_{j\neq i} \int d\mathbf{r}d\mathbf{r}'\frac{|\phi_i^*(\mathbf{r})|^2|\phi_j(\mathbf{r}')|^2}{|\mathbf{r} - \mathbf{r}'|}
\tag{II.5}
$$

The last term of Equation II.5 represents the Coulomb interaction energy, which is also referred as Hartree energy. Using the calculus of variations, with the constraint that the wave functions are orthonormal ($\int \phi_i^*\phi_j d\mathbf{r} = \delta_{ij}$) we minimize

with respect to the one-electron wavefunctions ϕ_i,

$$\frac{\delta}{\delta\phi_i}\left[\langle H\rangle - \sum_j \epsilon_j \int |\phi_j|^2 d\mathbf{r}\right] = 0, \tag{II.6}$$

where ϵ_j are the Lagrange multipliers. This reduces to the single particle Hartree equations

$$\left(-\frac{\nabla_i^2}{2} + V^{\text{ion}}\right)\phi_i(\mathbf{r}) + \sum_{j\neq i}\int d\mathbf{r}'\frac{|\phi_j(\mathbf{r}')|^2}{|\mathbf{r}-\mathbf{r}'|}\phi_i(\mathbf{r}) = \epsilon_i\phi_i(\mathbf{r}). \tag{II.7}$$

These equations can be solved self consistently to find the ground state many body wave function, ψ, and the ground state energy of the electrons can be calculated using Equation II.5.

The Hartree approximation in this form is not adequate for fermion systems, since the many body wavefunctions, ψ should be antisymmetric, thus Fock wrote the many body wave function in terms of antisymmetrized product of N one-electron wave functions, i.e., Slater determinant [12]

$$\psi = \frac{1}{\sqrt{N!}}\det\{\chi_1(\mathbf{r}_1), \chi_1(\mathbf{r}_2), ..., \chi_2(\mathbf{r}_1), ..., \chi_n(\mathbf{r}_n)\}, \tag{II.8}$$

where

$$\chi_i(\mathbf{r}_i) = \phi_i(\mathbf{r}_i)\sigma(s_i), \tag{II.9}$$

and $\sigma(s)$ represents the spin component which can be either up or down.

Following exactly the same procedure for minimizing the total energy with respect to the one-electron wavefunctions, results in the following set of one-electron equations which are known as the Hartree-Fock [13] equations

$$\left(-\frac{\nabla_i^2}{2} + V^{\text{ion}}\right)\phi_i(\mathbf{r}) \; + \; \sum_{j\neq i}\int d\mathbf{r}\frac{|\phi(\mathbf{r}')|^2}{|\mathbf{r}-\mathbf{r}'|}\phi_i(\mathbf{r}) \tag{II.10}$$

$$+ \; \sum_j \delta_{si,sj}\int d\mathbf{r}'\frac{\phi_i^*(\mathbf{r}')\phi_j(\mathbf{r}')}{|\mathbf{r}-\mathbf{r}'|}\;\phi_i(\mathbf{r}) = \epsilon_i\phi_i(\mathbf{r}).$$

The extra term in these equations, when compared to Equation (II.7), is known as the exchange energy term and is only non-zero when considering electrons of the same spin. It reduces the energy due to the antisymmetrization of the wave function by spatially separating the electrons of the same spin.

The Hartree-Fock energy is not the correct ground state energy, as one Slater determinant does not provide enough variational freedom to expand the entire Hilbert space of a set of fully interacting fermions. The difference between the total ground state energy and the Hartree-Fock energy is called correlation energy.

II.1.2   Density Functional Theory

Density functional theory was invented to overcome the problems of Hartree-Fock approximation. In density functional theory the minimization is done with respect to electron density rather than to the wave function itself.

In the following section we will discuss the density functional theory starting from the early attempts of Thomas and Fermi until the advanced Kohn-Sham model.

II.1.2.1   Thomas-Fermi Model

One of the early attempts to describe total energy of electrons as a function of electron density was the Thomas-Fermi (TF) model which was introduced in the year 1927 [14, 15].

Thomas and Fermi wrote the total kinetic energy of electrons as a functional

of electron density

$$\langle T \rangle = \frac{3}{10}(3\pi^2)^{2/3} \int d\mathbf{r} \rho(\mathbf{r})^{5/3}. \tag{II.11}$$

If we add nucleon-electron interaction and Hartree terms to the kinetic energy, we will get the Thomas Fermi energy

$$E^{\text{TF}} = \frac{3}{10}(3\pi^2)^{2/3} \int d\mathbf{r} \rho(\mathbf{r})^{5/3} + \int d\mathbf{r} \frac{\rho(\mathbf{r})Z}{|\mathbf{r} - \mathbf{R}|} + \int d\mathbf{r} d\mathbf{r}' \frac{\rho(\mathbf{r})\rho(\mathbf{r}')}{|\mathbf{r} - \mathbf{r}'|} \tag{II.12}$$

As we can see, TF model uses a crude approximation for kinetic energy. No contributions are coming from the exchange and correlation effects, which make it unapplicable to real problems. TF model fails to describe the binding of atoms and molecules and atomic shell structures. Another associated problem is that atoms get smaller with increasing atomic charge.

II.1.2.2 Kohn-Sham Theorem

Kohn and Sham [16, 17] introduced a more moderate density functional theory in 1964 in the form of two main theorems. In the first theorem they have proven that the ground state electron density uniquely determines the Hamiltonian operator and thus all the properties of the system, as they say in their paper *"we see that the full many particle ground state is a unique functional of $\rho(\mathbf{r})$"*. In the second theorem they proved that this functional which delivers the ground state energy of the system, delivers the lowest energy if and only if the input density is the true ground state density.

Kohn and Sham have written the total energy as a functional of electron

density as

$$E[\rho(\mathbf{r})] = \int d\mathbf{r}\rho(\mathbf{r})V^{\text{ext}} + F[\rho(\mathbf{r})].$$ (II.13)

This equation can be justified as an electron gas that exist in external potential V^{ext}, the external potential might be considered as ionic potential (V^{ion}) as in our previous notation. The other term is called the universal functional, which is independent of the external potential. It describes the electron-electron interaction including exchange-correlation terms plus the kinetic energy of electrons,

$$\hat{F}[\rho(\mathbf{r})] \quad = \quad \hat{T}^{\text{e}} + \hat{V}^{\text{el}-\text{el}}$$ (II.14)

$$= \quad \hat{T}^{\text{e}} + \hat{E}^{\text{H}} + \hat{E}^{\text{XC}}.$$ (II.15)

Writing the Kohn-Sham functional explicitly for an electron gas that exist in a background of positive ions as

$$E_{tot}[\rho(\mathbf{r})] = \frac{1}{2}\sum\int\phi_i^*(\mathbf{r})\nabla^2\phi_i(\mathbf{r})d\mathbf{r} \quad + \quad \int V^{\text{ion}}(\mathbf{r})\rho(\mathbf{r})d\mathbf{r} + \frac{1}{2}\int\frac{\rho(\mathbf{r})\rho(\mathbf{r}')d\mathbf{r}d\mathbf{r}'}{\mid\mathbf{r}-\mathbf{r}'\mid}$$
$$+ \quad E^{\text{XC}}[\rho(\mathbf{r})],$$ (II.16)

and using the same steps that was used before for Hartree and Hartree-Fock approximations, i.e., minimizing with respect to charge density instead of single particle wave functions and using the constraint that

$$\int\rho(\mathbf{r})d\mathbf{r} = N,$$ (II.17)

which introduces the Lagrange multiplier μ,

$$\frac{\delta}{\delta\rho}\left[E[\rho(\mathbf{r})] - \mu\int\rho(\mathbf{r})dr\right] = 0,$$ (II.18)

we get the Kohn-Sham equations

$$\left[-\frac{\nabla^2}{2} + V^{\mathrm{ion}}(\mathbf{r}) + V^{\mathrm{H}}(\mathbf{r}) + V^{\mathrm{XC}}(\mathbf{r})\right]\phi_i(\mathbf{r}) = \epsilon_i\phi_i(\mathbf{r}). \qquad \text{(II.19)}$$

Here ϕ_i is the wave function of electronic state i, ϵ_i are the Kohn-Sham eigenvalues, and V^{H} is the Hartree potential of the electrons given by

$$V^{\mathrm{H}}(\mathbf{r}) = \int \frac{\rho(\mathbf{r}')d\mathbf{r}'}{|\mathbf{r} - \mathbf{r}'|} \, . \qquad \text{(II.20)}$$

The exchange-correlation potential V^{XC} is the functional derivative of $E^{\mathrm{XC}}[\rho(r)]$,

$$V^{\mathrm{XC}}(\mathbf{r}) = \frac{\delta E^{\mathrm{XC}}[\rho(\mathbf{r})]}{\delta\rho(\mathbf{r})} \, . \qquad \text{(II.21)}$$

The Kohn-Sham equations represent a mapping of the interacting many-electron system into a system of noninteracting electrons moving in an effective potential due to all the other electrons.

II.1.2.3   Exchange and Correlation Functional

If the exchange-correlation energy functional were known exactly then we can find the exact ground state of the system as long as we do not use any approximations. Taking the functional derivative with respect to the density would produce an exchange-correlation potential that includes the effects of exchange and correlation exactly. But unfortunately this functional is not known explicitly, hence it must be approximated.

II.1.2.4   Local Density Approximation (LDA)

The simplest method of describing the exchange-correlation energy of an electronic system is to use the "local density approximation". In this approximation,

the exchange-correlation of an electronic system is constructed by assuming that the exchange-correlation energy per electron at point $\mathbf{r}$ in the electron gas, where $\epsilon^{XC}(\mathbf{r})$, is equal to the exchange-correlation energy per electron in homogenous electron gas that has the same density as the electron gas at point $\mathbf{r}$. Thus the exchange-correlation energy functional is given by

$$E^{XC}[\rho(\mathbf{r})] = \int \epsilon_{\text{hom}}^{XC}(\rho(\mathbf{r}))\rho(\mathbf{r})d^3\mathbf{r}, \tag{II.22}$$

where $\epsilon_{\text{hom}}^{XC}(\rho(\mathbf{r}))$ is the exchange and correlation function of a uniform electron gas of density $\rho(\mathbf{r})$.

This exchange-correlation functional will be formed from two terms, ϵ^X and ϵ^C terms. The E^X term is the exchange energy that appears in Hartree-Fock equations which is often called the Slater exchange term. E^X was originally derived by Bloch and Dirac in the late 1920s:

$$\epsilon^X = -\frac{3}{4}\left(\frac{3}{\pi}\right)^{\frac{1}{3}}\rho(\mathbf{r})^{\frac{1}{3}}. \tag{II.23}$$

Starting from Equation (II.23), Kohn and Sham [17], could derive an explicit expression for ϵ^X, given in Hartree units

$$\epsilon^X = -\frac{0.4582}{r_s}, \tag{II.24}$$

where r_s is the mean interelectronic spacing.

There is no such an explicit form for the ϵ^C but highly accurate numerical quantum Monte-Carlo simulations of the homogeneous electron gas are available from the work of Ceperley and Alder [18]. On the basis of their result, some parameterizations have been presented in literature for ϵ^C [19, 20]. One of these

parameterizations, which is going to be used throughout this thesis was reported by Pedrow and Wang in 1992 which takes the following form [20] in Hartree units.

$$\epsilon^{\mathrm{C}} = -2c_0(1 + \alpha_1 r_s)\ln\left[1 + \frac{1}{2c_0 + \beta_1 r_s^{1/2} + \beta_2 r_s + \beta_3 r_s^{3/2} + \beta_4 r_s^2}\right], \qquad \text{(II.25)}$$

where $c_0 = 0.031091$, $c_1 = 0.046644$, $\alpha_1 = 0.21370$, $\beta_1 = 7.5957$, $\beta_2 = 3.5876$, $\beta_3 = 1.6382$, $\beta_4 = 0.49294$.

II.1.2.5   Modifications to LDA

The local-density approximation, in principle ignores corrections to exchange-correlation energy at a point r due to nearby inhomogeneities in the electron density in the real solids. As a result, in order to achieve more accurate results, some modifications have been suggested which includes, the generalized gradient approximations (GGA) [21], weighted LDA [22], and self interaction correction [23].

II.1.3   Periodic Supercells

Using Kohn-Sham theorem it is possible to map the interacting many particle problem into equivalent noninteracting single particle problem. But the problem of handling an infinite number of noninteracting electrons moving in the static potential of an infinite number of nuclei or ions still remains to be solved. The problems that arise are that we have to calculate the wave function for each of the infinite number of electrons that exist in the entire solid, and the basis set required to expand each wave function is infinite. We can overcome these problem if we

perform the calculation by making use of using periodicity and applying Bloch's theorem to the electronic wave functions.

II.1.3.1   Bloch's Theorem

Bloch's theorem states that in a periodic solid each wave function can be written as the product of a cell-periodic part and a wavelike part,

$$\phi_i(\mathbf{r}) = \exp[i\mathbf{k} \cdot \mathbf{r}] f_i(\mathbf{r}). \tag{II.26}$$

The cell periodic part of the wave function can be expanded using a basis set of a discrete set of plane waves whose wave vectors are reciprocal lattice vectors of the crystal

$$f_i(\mathbf{r}) = \sum_{\mathbf{G}} c_{i,\mathbf{G}} \exp[i\mathbf{G} \cdot \mathbf{r}], \tag{II.27}$$

where the reciprocal lattice vectors $\mathbf{G}$ are defined by $\mathbf{G} \cdot \mathbf{R} = 2\pi n$ for all the $\mathbf{R}$ where $\mathbf{R}$ is a lattice vector of the crystal and n is an integer. Therefore each electronic wave function can be written as a sum of plane waves

$$\phi_i(\mathbf{r}) = \sum_{\mathbf{G}} c_{i,\mathbf{k}+\mathbf{G}} \exp[i(\mathbf{k} + \mathbf{G}) \cdot \mathbf{r}]. \tag{II.28}$$

II.1.3.2   Sampling the Brillouin Zone

Using Bloch's theorem the problem of calculating an infinite number of electronic wave functions is converted to the problem of calculating a finite number of wavefunctions at an infinite number of $\mathbf{k}$ points. Since under some symmetry consideration some $\mathbf{k}$ points will be identical, we can sample these $\mathbf{k}$ points in which case the total energy calculation will be performed on a finite number of

k points. Some methods have appeared in literature for sampling Brillouin zone and choosing special **k** points that can be used to calculate total energy with high accuracy [27-33], two of the most widely used in total energy calculations are Chadi and Cohen scheme [25] and Monkhorst-Pack scheme [26].

II.1.3.3   Monkhorst-Pack Scheme

One of the most popular schemes for generating k-points was proposed by [26]. This scheme, which was later modified to include hexagonal systems [27], produces a uniform grid of k-points along the three axes in reciprocal space.

The Monkhorst-Pack grid is defined by three integers, q_i where $i = 1, 2, 3$, which specify the number of divisions along each of the axes. These integers generate a sequence of numbers according to

$$u_r = (2r - q_i - 1)/2q_i, \tag{II.29}$$

where r varies from 1 to q_i. The Monkhorst-Pack grid is obtained from these sequences by equation

$$k_{prs} = u_p b_1 + u_r b_2 + u_s b_3. \tag{II.30}$$

This set of $q_1 q_2 q_3$ distinct points is further symmetrized and weights are assigned according to the number of symmetry images of a given point in the symmetrized set. It is possible to add a constant shift to all of the points in the set before symmetrization. This operation, when applied to hexagonal symmetry systems, results in a slightly modified recipe for the points along the a and b axes

$$u_p = (p - 1)/q_i. \tag{II.31}$$

19

II.1.3.4 Plane-Wave Representation of Kohn-Sham Equations

Using Bloch's theorem the electronic wave functions are expanded at each $\mathbf{k}$ point in terms of an infinite number of discrete plane waves. But since coefficients of plane waves $c_{i,\mathbf{k}+\mathbf{G}}$ with small kinetic energy $|\mathbf{k}+\mathbf{G}_c|^2$ are more important than those with large kinetic energy we can truncate the plane waves to include only plane waves that have kinetic energy less than some value of cutoff energy. This truncation of plane wave may result in some error however the error can be reduced by truncating plane waves at higher cutoff energy.

The inclusion of plane waves as a basis set for the electronic wave functions, will turn the Kohn-Sham equations into a simple form. Substitution of Equation (II.28) into Equation (II.19) and integration over $\mathbf{r}$ gives the secular equation

$$\sum_{\mathbf{G}}[|\mathbf{k}+\mathbf{G}|^2\delta_{\mathbf{G}\mathbf{G}'}+V^{\text{ion}}(\mathbf{G}-\mathbf{G}')+V^{\text{H}}(\mathbf{G}-\mathbf{G}')+V^{\text{XC}}(\mathbf{G}-\mathbf{G}')]c_{i,\mathbf{k}+\mathbf{G}'}=\epsilon_i c_{i,\mathbf{k}+\mathbf{G}}.$$

$$(\text{II.32})$$

In this form the kinetic energy is diagonal, and the various potentials are described in terms of their Fourier transformations. The solution of the above problem, whose size is determined by the choice of the cut-off energy $|\mathbf{k}+\mathbf{G}_\mathbf{c}|^\mathbf{2}$, can be achieved by matrix diagonalization. It must be noticed that inclusion of both valence and core electrons will result in a very large matrix, due to the large number of plane waves needed to expand the tightly bound core orbitals and to follow the rapid oscillations of the wave functions of the valence electrons in the core region. The usage of pseudopotential instead of the true ionic potential can eliminate this problem.

II.1.4 Pseudopotential Approximation

Since most of the physical properties of solids depend on the valence electrons more than core electrons, the pseudopotential technique removes the core electrons and the strong coulomb ionic potential V^{ion} and replaces them by a weaker pseudopotential, V^{PS}, in which case it will act on a set of pseudowavefunctions, ϕ^{PS}, rather than the true all electron wavefunctions ϕ^{AE}.

The pseudowavefunctions and the true wavefunctions should be identical outside a chosen core cutoff radius

$$\phi^{\mathrm{PS}}(\mathbf{r}) \rightarrow \phi^{\mathrm{AE}}(\mathbf{r}) \quad r > r^c \tag{II.33}$$

and are normalized

$$\int_0^\infty \left|\phi^{\mathrm{PS}}(\mathbf{r})\right|^2 = \int_0^\infty \left|\phi^{\mathrm{AE}}(\mathbf{r})\right|^2 d\mathbf{r} = 1, \tag{II.34}$$

which implies the norm-conserving constraint

$$\int_0^{r^c} \left|\phi^{\mathrm{PS}}(\mathbf{r})\right|^2 d\mathbf{r} = \int_0^{r^c} \left|\phi^{\mathrm{AE}}(\mathbf{r})\right|^2 d\mathbf{r}. \tag{II.35}$$

The equality of true and pseudowavefunctions outside the core region will result in an identical density outside the core region. The norm-conserving condition insures that electronic density will be the same also in the core region which is important to reproduce the scattering properties in the core region. Since the phase shift produced by the ion core is different for each angular-momentum component of the valence wave function, the scattering properties inside the core region will be angular-momentum-dependent, which makes it important to

have angular-momentum-dependent pseudopotential, thus the pseudopotentials are constructed in terms of angular momentum nonlocal operator

$$V^{PS} = \sum_{lm} |Y_{lm} > V_l^{PS} < Y_{lm}|, \tag{II.36}$$

where Y_{lm} are spherical harmonics and V_l is the angular momentum component of the pseudopotential acting on the wavefunction. Pseudopotentials of this type are known as a "non-local norm-conserving pseudopotentials" and are "transferable" since they are capable of describing the scattering properties of an ion in a variety of atomic environments.

II.1.4.1   Constructing the Pseudopotential

The generation of pseudopotential [31] must be done self consistently, using density functional theory to model electron-electron interaction, using specific LDA or GGA exchange and correlation functional approximation E^{XC}. It is worth to say here that the E^{XC} functional used in generating pseudopotential and the one used in polyatomic calculation must be identical.

The first step in generating the pseudopotential is to do all electronic calculation for a single atom assuming spherical symmetry of Schrödinger equation for simplicity. The relativistic effects can be counted for by using scalar-relativistic kinetic energy operator [32]. Relativistic effects become more important in describing heavier atoms.

All inclusive electronic calculations for single atoms will generate the atomic wave-functions for all of its electrons, and consequently the all-electron density,

and the corresponding all-electron orbital energies. The second step is the generation of a screened pseudopotential, which is an intermediate step toward norm-conserving pseudopotential. For the screened pseudopotential expression one may choose between two commonly used schemes, either by Hamman [33] or by Troullier and Martins (TM) [34]. The choice of screening scheme depends on the elements under consideration. TM scheme produces softer pseudopotentials for $2p$, and $3d$, $4d$, $5d$ valence states of the first row, and of the transition metal elements, respectively, while for other elements the two schemes behave alike.

The final ionic pseudopotential, which can be used in polyatomic calculations, is derived by subtracting the electrostatic and the exchange-correlation screening contributions due to the valence electrons from the screened pseudopotential.

It should be noted here that the final ionic pseudopotential includes the exchange-correlation energy E^{XC} between the valence and core electrons as a term which depends linearly on the valence density ρ^{PS}. In some cases, however, this is not preferable, since E^{XC} might depend on valence electron density in a nonlinear way. For instance, in systems involving alkali atoms with soft electrons, the nonlinearity of this term becomes more important and therefore nonlinear core-valence exchange correlation approximation must be used instead. The non-linearity of E^{XC} can be achieved by following the recipe of Louie *et al.* [35]. By adding a partial core density ρ^{core}, this will reproduce the full core charge density ρ^{core} outside a chosen cutoff radius r^{nlc}, but it will be a smoother function inside, which makes it easier to use together with plane waves.

II.1.4.2 Kleinman-Bylander Form of Pseudopotential

Since the pseudopotential will be identical to the Coloumb potential at large radius getting independent of l, it is reasonable for computational efficiency to construct the pseudopotential in semilocal form, in which case we will have multiplicative local potential plus only a few l-dependent short-range corrections for $l < l_{max}$

$$
\begin{aligned}
\langle \mathbf{r} \mid \hat{V}^{\mathrm{PS}} \mid \mathbf{r}' \rangle &= \langle \mathbf{r} \mid \hat{V}^{\mathrm{LOC}} + \hat{V}^{\mathrm{SL}} \mid \mathbf{r}' \rangle \qquad\qquad\qquad\qquad (\mathrm{II.37}) \\
&\to V_{l_{\mathrm{loc}}}^{\mathrm{PS}}(\mathbf{r})\delta(\mathbf{r} - \mathbf{r}') + \sum_{l=0}^{l_{\max}} \sum_{m=-l}^{m=l} Y_{lm}^{*} \delta V_{l}^{\mathrm{PS}}(\mathbf{r}) \frac{\delta(\mathbf{r} - \mathbf{r}')}{r^2} Y_{lm},
\end{aligned}
$$

where the pseudopotential is written in terms of local component $V^{\mathrm{LOC}}(\mathbf{r})$ taken as one component of the semilocal components of pseudopotential, $V_{l_{\mathrm{loc}}}^{\mathrm{PS}}(r) = V_{l=\mathrm{loc}}^{\mathrm{PS}}(r)$, the second term which is more important in the core region is l-dependent component $\delta V_{l}^{\mathrm{PS}}(\mathbf{r}) = V_{l}^{\mathrm{PS}}(\mathbf{r}) - V^{LOC}(\mathbf{r})$ which are confined to core region and eventually vanish beyond r_{l}^{c}. The number of projections in the second term can be reduced if one sets the maximum l component of the pseudopotential as local potential in which case $V^{\mathrm{LOC}}(\mathbf{r}) = V_{l_{\mathrm{loc}}}^{PS}(\mathbf{r}) = V_{l_{\max}}^{PS}$

The computational load can be reduced further if one uses the fully separable pseudopotential form of Kleinman and Bylander [36], a widely used technique in most *ab initio* codes

$$
\langle \mathbf{r}|\hat{V}^{\mathrm{PS}}|\mathbf{r}' \rangle = \langle \mathbf{r}|\hat{\mathbf{V}}^{\mathrm{LOC}} + \delta\hat{\mathbf{V}}^{\mathrm{KB}}|\mathbf{r}' \rangle. \qquad\qquad (\mathrm{II.38})
$$

Starting from a semi-local pseudopotential, the corresponding KB pseudopotential constructed in such a way that it yields the same pseudowavefunction and

energies using specific projector functions [36].

In the polyatomic calculations, the Kleinman-Bylander form reduces the computation load considerably. In semi-local form the evaluation and storage of $(N^2 + N)/2$ matrix elements are required, N being the number of basis sets, whereas in KB form only N matrix elements are required to be evaluated and stored. In transforming the semi-local to the corresponding KB pseudopotential one needs to make sure that KB form does not lead to unphysical "ghost" states at energies near or below valence states as those may undermine its transferability. The ghost states might be avoided by proper choice of the local component l_{loc} and the core cutoff radii r_l^c in the basic semi-local pseudopotential [31].

II.1.4.3 Transferability of the Pseudopotential

The transferability of the pseudopotential depends crucially on the proper choice of cutoff radius, an adequate account of nonlinear exchange-correlation interaction between core and valence electrons, the quality of Kleinman-Bylander form of pseudopotential, the validity of frozen-core approximation and the treatment of higher angular momentum components [31].

In general increasing r_l^c yields a softer pseudopotential, which converges more rapidly for a plane wave basis set, but the pseudopotential will be less transferable as it becomes less accurate at radii relevant to bonding. In decreasing its value, care must be taken since it must be larger than the radius of the outermost radial node in the all electron orbital r_l^{max}, otherwise, the potential will be very poor. In the Hamman scheme, as a rule of thumb one may set r_l^c equal to $0.6 r_l^{\mathrm{max}}$ if

there are core states present with the same angular momentum, and to $0.4r_l^{\mathrm{max}}$ if otherwise. In the case of Truiller-Martin scheme, on the other hand, r_l^c is usually $1.33 - 4$ times larger [31].

II.1.4.4 Ultrasoft Pseudopotentials

If the pseudo-wave-functions are allowed to be as soft as possible within the core region, the cutoff energy can be reduced dramatically. In order to achieve this, a generalized orthogonality condition should be introduced, then the electron density has to be augmented in the core region in order to recover the full electronic charge. As a result the electron density will be subdivided into a smooth part that extends throughout the unit cell, and a hard part localized in the core, such types of pseudopotential are known as ultrasoft pseudopotentials (USP) [37].

II.1.5 Total Ionic Potential

After generating the pseudopotential, it should be placed in position with each ion in the solid. Usually the information about the ionic positions come from the structure factor

$$S_\alpha(\mathbf{G}) = \sum_I \exp[i\mathbf{G} \cdot \mathbf{R}_I].\tag{II.39}$$

The total ionic potential will then be obtained by summing the product of the structure factor and pseudopotential over all ions [38].

II.1.6   Minimization Techniques

Equation (II.19) has to be solved self consistently in order to find the correct charge density and hence the ground state energy. The methods which are used for this purpose are classified into two main classes: (a) indirect minimization techniques as used in matrix-diagonalization and Car-Parrinello methods, and (b) direct minimization techniques as used in steepest decent and conjugate gradient methods. In the following section these methods will be discussed briefly.

II.1.6.1   Matrix Diagonalization

The first method to be used in solving Kohn-Sham equations was the conventional matrix diagonlization. This method proceeds by an initial guess for the electronic charge density from which Hartree potential and the exchange-correlation potential can be constructed. The Hamiltonian matrix is then calculated for each $\mathbf{k}$ point as in Equation (II.19). Diagonilizing this matrix will give the eigenvalues and eigenstates. From the output the charge density is calculated and used again as an input to restart the cycle. This procedure will be repeated until the input and output charge densities approach to each other. In some cases this input electronic charge density is taken to be as a combination of the new and the old one, which is known as "charge mixing", for accelerating the convergence. The drawback of this method is that the CPU time scales with the third power of the number of plane waves in the basis set, as well as the memory requirement scales with square of the number of plane wave basis set, which restricts the number of

atoms inside the unit cell to be in the order of 10 atoms [38].

II.1.6.2 Car-Parrinello Method

Car and Parrinello [39] introduced an alternative way of solving Kohn-Sham equations without the usage of matrix diagonalization. Their method works by treating the coefficients of electronic wave functions as dynamical variables, and allowing for their evolution in time using molecular dynamics algorithms, until they eventually converge to the Kohn-Sham eigenstates.

They defined a lagrangian for the electronic system as follows

$$L = \sum_i \mu < \dot{\phi}|\dot{\phi} > - E[\{\phi_i\}, \{\mathbf{R}_I\}, \{\alpha_n\}] + \sum_{i,j} \Lambda_{ij} \left[\left\{ \int \phi_i^* \phi_j d^3\mathbf{r} \right\} - \delta_{ij} \right], \quad \text{(II.40)}$$

where μ is a fictitious mass associated with the electronic wave functions, E is the Kohn-Sham energy functional, $\mathbf{R}_I$ is the position of ion I, and α_n define the size and the shape of unit cell. The kinetic energy term in the Lagrangian is due to the fictitious dynamics of the electronic degrees of freedom.

The Kohn-Sham energy functional takes the place of potential energy in conventional Lagrangian formulation. The Lagrange multipliers Λ_{jj} ensures that the wave functions remain normalized, while Lagrange multipliers Λ_{ij} ensures that the wave functions remain orthogonal.

The equation of motion for the electronic states are derived from the Lagrange equations of motion,

$$\frac{d}{dt} \left[\frac{\partial L}{\partial \dot{\phi}^*} \right] = \frac{\partial L}{\partial \phi^*} \quad \text{(II.41)}$$

which gives

$$\mu\ddot{\phi}_i = -H\phi_i + \sum \Lambda_{ij}\phi_j, \qquad\qquad \text{(II.42)}$$

where H is the Kohn-Sham Hamiltonian.

The second term adds forces $\Lambda_{ij}\phi_j$ to the force $-(H\phi_i)$. These forces ensure the electronic wave functions remain orthonormal at every instant of time. The molecular dynamics evolution of the electronic wave functions under these equations of motion would also conserve the total energy in the electronic degrees of freedom for the system of fixed ions. The evolution of the electronic wave functions with time requires the evolution of the multipliers at each time step. However in simulation they are taken to be constant during the time steps, which cause the wave functions to be not exactly orthonormal at the end of the time step. As a result sperate orthonormalization is needed in the calculation at the end of each time step. This makes it reasonable to eliminate the constraints of orthonormality from the equation of motion, and to impose orthonormality after the equations of motion are integrated at each time step.

Lagrange multipliers are approximated by the expectation values of the energies of the states, λ_i, where

$$\lambda_i = <\phi_i|H|\phi_i> . \qquad\qquad \text{(II.43)}$$

This leads to an equation of motion that has the form

$$\mu\ddot{\phi} = -[H - \lambda_i]\phi_i. \qquad\qquad \text{(II.44)}$$

After the accelerations of the wave functions are found, the equations of motion can be integrated in time, either using Verlet algorithm or high order schemes.

Care must be taken when choosing the time step, since it may effect the stability of the evolution. A typical time step that is allowed for stability must be

$$\triangle t \approx \frac{2\mu^{1/2}}{(\epsilon_{\max} - \epsilon_{\min})^{1/2}} \tag{II.45}$$

where $\epsilon_{\max}$, $\epsilon_{\min}$ are the largest and smallest eigenvalues of the of the problem respectively. Since $\epsilon_{\max}$ can increase with the energy cut-off of the basis set, it means that δt should be reduced as the energy cutoff increases.

Another limitation imposed on the time step is due to the instabilities caused by charge fluctuations or " charge sloshing". Since electron density changes at each time step, the Hartree and exchange-correlation functions must be updated on each time step also. This may cause instability if the changes are too large which makes it necessary to reduce the time step. " Charge sloshing" also appears when the length of super cell is very long, which can be a major difficulty when studying larger systems [38].

II.1.6.3 Steepest Decent Method

Steepest decent (SD) method [38] works by minimizing any function directly, i.e, we search for the minimum point on the function by following suggested direction.

Starting from a random point x^1 on a function $F(x)$, we can minimize this function by moving along the steepest decent direction, i.e., along the negative of the gradient at that point which is given by

$$g^1 = -\nabla F|_{x=x^1}. \tag{II.46}$$

After finding the direction of steepest decent, one has to move along the line

that goes in the steepest direction, to the point $x^1 + bg^1$ where the function is minimum, from which we can establish another steepest decent direction trying to find the point which minimizes the function along the new line. Repeating this process, one may reach the global minimum of the function. A good way of finding b that minimizes the function along any line, is by locating the point at which the gradient is orthogonal to search line. i.e., b has to satisfy $g^1.\nabla F(x^1 + bg^1) = 0$.

The drawback of this method is that sometimes it may require very large number of iterations (searching lines) in order to locate the global minimum.

II.1.6.4 The Conjugate-Gradient Method

The starting point of Conjugate-Gradient (CG) methods [38] is exactly similar to SD method. But the only difference is that searching directions, d^1 and d^2 must be conjugate, i.e, the relation $d^1.\nabla.d^2 = d^2.\nabla.d^1 = 0$, must be satisfied, or in general $d^n.\nabla.d^m = d^m.\nabla.d^n = 0$ for $n \neq m$, where n, m denote successive steps. The research directions in this method are obtained from the following algorithm

$$d^m = g^m + \gamma^m d^{m-1} \tag{II.47}$$

and

$$\gamma^m = \frac{g^m g^m}{g^{m-1} g^{m-1}} \tag{II.48}$$

and $\gamma^1 = 0$. g is the steepest decent search direction as given by Equation (II.46).

The difference between conjugate gradient methods and steepest decent is that, in steepest decent the search direction depends on the present point, while in CG method it depends on the information obtained from all the sampling

31

points.

CG methods can be used successfully to minimize Kohn-Sham equations without encountering problems associated with the unit cell size or energy cutoff as was stated with Car-Parrinello, which enables the *ab initio* methods to study larger systems. Another advantage is that it can be implemented in molecular dynamics simulations in which case the time step can be in the same order of that used in classical simulations.

II.1.7 Hellmann-Feynman Forces

The force on any ion I, $\mathbf{F}_I$ can be calculated by taking the derivative of the total energy with respect to the ionic positions

$$\mathbf{F}_I = -\frac{dE}{d\mathbf{R}_I} \tag{II.49}$$

As the ions move, the wave functions must be changed to their self consistent eigenstates corresponding to the new positions. The change in the electronic wave functions will contribute the force on the ion by this equation

$$\mathbf{F}_I = -\frac{\partial E}{\partial \mathbf{R}_I} - \sum_i \frac{\partial E}{\partial \phi_i} \frac{\partial \phi_i}{\partial \mathbf{R}_I} - \sum_i \frac{\partial E}{\partial \phi_i^*} \frac{\partial \phi_i^*}{\partial \mathbf{R}_I} \tag{II.50}$$

It should be noted here that if ϕ_i was an eigenstate of the Hamiltonian then the sum of last two terms in the last equation will be zero and the force will reduce to

$$\mathbf{F}_I = -\frac{\partial E}{\partial \mathbf{R}_I} \tag{II.51}$$

This result is known as Hellmann-Feynman theorem [40], which states that the physical force on any ion will simply be the partial derivative of the total

energy with respect to the ionic position, provided that the eigenstates are very close to the ground state, otherwise there will be an error that may take the ions away from the global minima in dynamical simulation algorithms [38].

II.2 Empirical potential energy functions

Another method of calculating total energy of a system of atoms, is to use empirical many body potential energy functions. These functions are designed in such a way that they include all the electronic interactions implicitly, in a simple formulation. The functions, which usually come as a function of nuclear coordinates, are parametrized to fit to some empirical data or density functional database.

The empirical potential energy functions are used extensively in atomistic computer simulations, especially in molecular dynamics and in Monte Carlo simulations. Not surprisingly, because of its technological importance, silicon has been the prototype material for developing many empirical potentials [41]. These potentials differ in their degrees of sophistication, functional forms, and ranges of interaction. Many of these potentials were employed to investigate the structures and energetics of Si clusters as well as bulk phases, and surfaces. In our work we will use the potential developed by Stillinger-Weber [8].

II.2.1 Stillinger-Weber Potential

F. Stillinger and T. Weber developed this potential [8] for liquid silicon in 1985, and henceforth it was used very extensively in simulations, being the most common potential for tetrahedrally bonded structures. In 1986, Ding and Anderson

have parameterized this potential to give the structural properties of a-Ge and c-Ge [42]. The potential was used also to simulate mixed systems of Si and Ge [43]. The potential consist of two parts, pair potential and three body terms

$$\Phi = \Phi_2 + \Phi_3 = \sum U_{ij} + \sum W_{ijk}, \qquad \text{(II.52)}$$

where U_{ij} and W_{ijk} represent the pair and three body terms respectively. In terms of energy and length units ϵ and σ , we can write

$$U_{ij} = \epsilon f_2 \left(\frac{r_{ij}}{\sigma} \right), \qquad \text{(II.53)}$$

$$W_{ijk} = \epsilon f_3 \left(\frac{r_i}{\sigma}, \frac{r_j}{\sigma}, \frac{r_k}{\sigma} \right), \qquad \text{(II.54)}$$

f_2 Is a function of only scalar distance, whereas f_3 must possess full transitional and rotational symmetry,

$$f_2(r) = \begin{cases} A(Br^{-p} - r^{-q}) \exp[(r-a)^{-1}] & , r \leq a \\ \\ 0 & , r \geq a \end{cases} \qquad \text{(II.55)}$$

Where A, B and p are positive and r_{ij} is given by $|\mathbf{r}_i - \mathbf{r}_j|$. The generic form automatically cuts off at $r = a$ without discontinuities in any derivatives, which is a distinct advantage in any molecular dynamics simulation. One has the same cut off advantage for the case of three body interaction f_3

$$f_3(r_i, r_j, r_k) = h(r_{ij}, r_{ik}, \Theta_{ijk}) + h(r_{ji}, r_{jk}, \Theta_{jik}) + h(r_{ki}, r_{kj}, \Theta_{ikj}), \qquad \text{(II.56)}$$

where Θ_{ijk} is the angle between r_{ij} and r_{ik} subtended at vertex i , etc., provided that r_{ij} and r_{ik} are less than the previously introduced cut off a and it has the following form

$$h(r_{ij}, r_{ik}, \Theta_{ijk}) = \lambda \exp[\gamma(r_{ij} - a)^{-1} + \gamma(r_{ik} - a)^{-1}] \left(\cos \Theta_{ijk} + \frac{1}{3} \right)^2. \qquad \text{(II.57)}$$

In table II.2.1, the empirical parameters of the SW potential are listed for Si and Ge.

Table II.1: The parameters for SW potential for Si and Ge

Parameter	Si	Ge
A	7.049556	7.049556
B	0.602224	0.602224
p	4	4
q	0	0
a	1.8	1.8
γ	1.2	1.2
λ	21.0	31.0
σ	2.0951	2.1810
ϵ	2.17 eV	1.91 eV

II.3 Dynamical Simulation Methods

Whichever method was used for calculating the total energy and forces of the system, the empirical potential, or the *ab initio* density functional, it is important usually to allow for dynamical evolution of the ionic system in time.

There are well developed methods that allow for this dynamical simulation. Molecular dynamics and Monte Carlo stand as the most important ones that are extensively used in condensed matter physics.

II.3.1 The Method of Molecular Dynamics

The molecular dynamics method (MD) was first introduced by Alder and Wainwright in the late 1950's [44] to study the interactions of hard spheres. Many important insights concerning the behavior of simple liquids emerged from their studies. The next major advance was in 1964, when Rahman carried out the first simulation using a realistic potential for liquid argon [45]. The first molecular dynamics simulation of a realistic system was done by Rahman and Stillinger in their simulation of liquid water in 1974 [46]. In the last decades MD was successfully used in solid state physics to study crystalline, liquid, and amorphous systems as well as surfaces, adsorption and growth.

II.3.1.1 MD Formalism

The starting point for a MD method is a well defined microscopic description of a physical system of atoms or molecules that obey classical laws of motion. The description can be introduced via a Lagrangian or a Hamiltonian from which Newton's equations of motion can be expressed. The main task of MD will be to compute the phase trajectories of a collection of molecules or atoms - finding positions and momenta for each molecule or atom as a function of time - from which one can obtain the static as well as the dynamic properties of the system [47].

If we start by the many body Hamiltonian

$$\mathcal{H} = \frac{1}{2} \sum_i \frac{1}{m} p_i^2 + \sum_{i<j} u(r_{ij}), \qquad (\text{II.58})$$

we get the equations of motion for particle i

$$m\frac{d\mathbf{r}_i}{dt} = \mathbf{p}_i, \tag{II.59}$$

$$\frac{d\mathbf{p}_i}{dt} = \sum_j \mathbf{F}(\mathbf{r}_{ij}). \tag{II.60}$$

To solve the above two equations on a computer, we construct a finite difference scheme for the differential equations to the highest possible order. From the difference equation we then derive the recursion relations for the positions and velocities. The recursion relations give us the solution of the above equation in a step by step manner, i.e., if we know the position and velocity at some time step t, we will be able to find the position and velocity at a later time step $t + h$. The time step interval will depend on the algorithm used, but in any case, it will be smaller than the physical time taken for a molecule to travel its own length [48].

II.3.1.2 Predictor-Corrector Algorithms

Predictor-corrector methods were first introduced into molecular dynamics by Rahman [44]. Generally, these methods are composed of three steps: prediction, evaluation, and correction. In particular, from the current position, $\mathbf{r}(t)$, and velocity, $\mathbf{v}(t)$, the steps are as follows:

1. Predict the position $x(t + \Delta t)$ and velocity $v(t + \Delta t)$ at the end of the next step.

2. Evaluate the forces at $t + \Delta t$ using the predicted position.

3. Correct the predictions using some combination of the predicted and previous values of position and velocity

II.3.1.3   Gear's Predictor-Corrector Algorithms

The predictor-corrector algorithms that are usually used in MD are usually based on a collection of methods devised by Gear [49]. The one which is going to be used in this work is based on following steps:

Predict molecular positions $\mathbf{r}_i$ at time $t + \Delta t$ using a fifth order Taylor series based on positions and their derivatives at time t. Thus the derivatives $\dot{\mathbf{r}}_i, \ddot{\mathbf{r}}_i, \mathbf{r}_i^{iii}, \mathbf{r}_i^{iv}$ and $\mathbf{r}_i^{v}$ are needed at each time step, which are also predicted at time $t + \Delta t$ by applying Taylor series at t

$$
\begin{aligned}
\mathbf{r}_i(t + \Delta t) &= \mathbf{r}_i(t) + \dot{\mathbf{r}}(t)\Delta t + \ddot{\mathbf{r}}_i(t)\frac{(\Delta t)^2}{2!} + \mathbf{r}_i^{(iii)}(t)\frac{(\Delta t)^3}{3!} + \mathbf{r}_i^{(iv)}(t)\frac{(\Delta t)^4}{4!} \\
&\quad + \mathbf{r}_i^{(v)}(t)\frac{(\Delta t)^5}{5!} \tag{II.61}
\end{aligned}
$$

$$
\begin{aligned}
\dot{\mathbf{r}}_i(t + \Delta t) &= \dot{\mathbf{r}}_i(t) + \ddot{\mathbf{r}}_i(t)\Delta t + \mathbf{r}_i^{(iii)}(t)\frac{(\Delta t)^2}{2!} + \mathbf{r}_i^{(iv)}(t)\frac{(\Delta t)^3}{3!} \\
&\quad + \mathbf{r}_i^{(v)}(t)\frac{(\Delta t)^4}{4!} \tag{II.62}
\end{aligned}
$$

$$
\ddot{\mathbf{r}}_i(t + \Delta t) = \ddot{\mathbf{r}}_i(t) + \mathbf{r}_i^{(iii)}(t)\Delta t + \mathbf{r}_i^{(iv)}(t)\frac{(\Delta t)^2}{2!} + \mathbf{r}_i^{(v)}(t)\frac{(\Delta t)^3}{3!} \tag{II.63}
$$

$$
\mathbf{r}_i^{(iii)}(t + \Delta t) = \mathbf{r}_i^{(iii)}(t) + \mathbf{r}_i^{(iv)}(t)\Delta t + \mathbf{r}_i^{(v)}(t)\frac{(\Delta t)^2}{2!} \tag{II.64}
$$

$$
\mathbf{r}_i^{(v)}(t + \Delta t) = \mathbf{r}_i^{(iv)}(t) + \mathbf{r}_i^{(v)}(t)\Delta t \tag{II.65}
$$

$$
\mathbf{r}_i^{(v)}(t + \Delta t) = \mathbf{r}_i^{(v)}(t). \tag{II.66}
$$

After predicting the coordinates of the atoms by the above equations, the forces can be evaluated on each molecule at time $t + \Delta t$ using the predicted positions. Then the predicted positions and their derivatives can be corrected using the discrepancy $\Delta\ddot{\mathbf{r}}$ between the predicted acceleration and that given by the evaluated force $\mathbf{F}_i$. The difference between the predicted acceleration and the evaluated is

then formed

$$\Delta\ddot{\mathbf{r}} = [\ddot{\mathbf{r}}(t + \Delta t) - \ddot{\mathbf{r}}^P(t + \Delta t)]. \tag{II.67}$$

In Gears algorithm for second order differential equations this difference term is used to correct all the predicted positions and their derivatives, thus

$$
\begin{aligned}
\mathbf{r}_i(t) &= \mathbf{r}_i^P(t) + \alpha_0 \Delta R_2 \\[1mm]
\dot{\mathbf{r}}_i(t)\Delta t &= \dot{\mathbf{r}}_i^P(t)\Delta t + \alpha_1 \Delta R_2 \\[1mm]
\frac{\ddot{\mathbf{r}}_i(t)(\Delta t)^2}{2!} &= \frac{\ddot{\mathbf{r}}_i^P(t)(\Delta t)^2}{2!} + \alpha_2 \Delta R_2 \\[1mm]
\frac{\mathbf{r}_i^{(iii)}(t)(\Delta t)^3}{3!} &= \frac{\mathbf{r}_i^{(iii)P}(t)(\Delta t)^3}{3!} + \alpha_3 \Delta R_2 \\[1mm]
\frac{\mathbf{r}_i^{(iv)}(t)(\Delta t)^4}{4!} &= \frac{\mathbf{r}_i^{(iv)P}(t)(\Delta t)^4}{4!} + \alpha_4 \Delta R_2 \\[1mm]
\frac{\mathbf{r}_i^{(v)}(t)(\Delta t)^5}{5!} &= \frac{\mathbf{r}_i^{(v)P}(t)(\Delta t)^5}{5!} + \alpha_5 \Delta R_2,
\end{aligned}
\tag{II.68}
$$

where

$$\Delta R_2 = \frac{\Delta\ddot{\mathbf{r}}(\Delta t)^2}{2!}, \tag{II.69}$$

and α_i are $\frac{3}{20}, \frac{251}{360}, 1, \frac{11}{18}, \frac{1}{6}, \frac{1}{60}$ for i equal to $0, 1, 2, 3, 4, 5$, respectively.

II.3.1.4 The Other Algorithms

The simplest finite difference method that has been widely used in molecular dynamics is a third order one known as Verlet algorithm [50]. Verlet has combined two third order Taylor expansions for atomic positions with one step ahead and one step back. The algorithm that will appear out of these expansions will require to provide the atomic positions for the first two time steps which make it non self starting, besides the velocities are not evaluated at the same time step as positions. Later on Swope *et al.* [51] have proposed an equivalent algorithm that does

store the positions and velocity at the same time step, besides, it is self starting. Another modification to the basic Verlet algorithm is the so called "Leap-Frog" scheme [52], in which the current positions, the accelerations, together with a previous mid-step velocity are stored, then the velocity is calculated at later half-time step leaping over the coordinates.

II.3.1.5   Constant-Temperature MD

Many methods have been proposed for simulating physical systems at constant temperature. Anderson [53] has proposed a method in which at some time intervals, the velocity of randomly selected particle or particles are chosen fresh from Maxwell-Boltzman distribution. Nose [54] have proposed another method in which he introduced another degree of freedom which represents the reservoir with a conjugate momentum. The energy in this method is allowed to flow dynamically from the reservoir to the system and back, in a similar manner like controlling the volume of a sample by using a piston. In 1985 Hoover [55] have extended the analysis of Nose method introducing friction coefficient that act like a Lagrangian multiplier, a method which is known as Nose-Hoover thermostat. A more simple choice for fixing temperature is to fix the kinetic energy to a given value corresponding to the desired temperature through the course of simulation [47]

$$\Lambda = \frac{1}{2} \sum_i m v_i^2 = \text{const.} \tag{II.70}$$

This can be achieved by rescaling the atom velocities by a factor β. Since we require that the system to have zero total linear momentum, this removes three

degrees of freedom, the constraint of constant kinetic energy removes one more degree of freedom. Hence the scaling factor is

$$\beta = [(3N - 4)K_{\mathrm{B}}T / \sum_i mv_i^2]^{(1/2)}, \qquad (\text{II.71})$$

and after the scaling step we will have

$$\frac{1}{2} \sum_i mv_i^2 = \frac{1}{2}(3N - 4)K_{\mathrm{B}}T. \qquad (\text{II.72})$$

II.3.1.6   The Other Ensembles

Some algorithms were developed for simulating some other ensembles like isothermal-isobaric ensembles. Such ensembles can be interesting for computation of certain quantities and comparison with experimental observations, like specific heat at constant pressure (Cp). In such ensembles, the internal total energy is no longer a conserved quantity but instead the enthalpy;

$$H = E + P_{\mathrm{ext}}V, \qquad (\text{II.73})$$

where P_{ext} is the external applied pressure. The algorithms deal with the ensemble introducing the volume as dynamical variable, allowing it to change in order to achieve constant pressure. The change in volume may be isotropic [53], or anisotropic [56], where the latter case might be important in studying the phase changes in solids.

CHAPTER III

Mg ADSORPTION ON Si(001) SURFACE

Adsorption of overlayers of Mg atoms on silicon surfaces has been a subject of growing interest during the last decade because of its importance in technological applications such as the efficient photocathodes and thermionic energy converters. Even though several experimental and theoretical studies have been carried out for studying the Mg/Si(111) systems [57] only few have been reported for the adsorption of Mg on Si(001) surfaces [58-64]. The understanding of Mg adsorption on Si(001) has become especially an interesting problem to investigate because of the possible use of Si substrates for the growth of Mg_2Si films. More recently, after the report of superconductivity in MgB_2, its growth on Si(001) surfaces [65, 66] has become a current issue.

One of the earliest experiments of Mg adsorption on Si(001) were carried out by Kawashima *et al.* [59], who have obtained LEED and AES results starting from full coverage to lower coverages by allowing for thermal desorption. They observed

that as the coverage decreased the various structural phases appeared in the order 1×1, 2×3, 2×2, another 2×3, and finally the clean 2×1 which correspond to the coverages of 1, 1/3, 1/4, 1/6, and 0 ML, respectively. They concluded that Mg atoms were adsorbed on hollow site (valley-bridge site, in their notation) for each coverage mentioned above.

Hutchison *et al.* [60], in their STM results for the low coverage-Mg/Si(001) case, have reported three types of adsorption geometries at room temperature. Type I is the most favorable phase and it refers to a single Mg atom adsorbed on a cave site. The least frequently observed type II, being a localized phase, corresponds to two Mg atoms adsorbed on cave sites to relieve the stress on the chain of type I phases. Type III phase, which may occur everywhere but next to a type II phase, contains multiple Mg adatoms (three at most) adsorbed on a combination of adjacent sites.

Similar observations also with the use of STM have been reported by Kubo *et al.* [61] for Mg adsorption at room temperature. However, they speculated another interpretation differing from that of Hutchison *et al.*, such that according to Kubo *et al.*, type I may correspond to two Mg atoms adsorbed on adjacent hollow sites and type III may correspond to a single Mg atom adsorbed on a pedestal site. In addition, for the annealed case at high temperature, they have tentatively suggested two models possessing the 2×2 symmetry by incorporating an extra Si on the shallow site (see Figure III.2) bonding to Mg adatom. The first model consists of a single Mg atom adsorbed on the neighboring shallow site bonding across the hallow site, and second one consists of two Mg atoms adsorbed

on cave sites on each side of the extra Si atom.

Kim *et al.* [62] have reported in their LEED data that the 2×2 reconstruction corresponding to 1/2 ML coverage occurs at 280°C, whereas for 1/3 ML coverage with 2×3 symmetry occurs at 390°C showing the dependence of surface reconstruction on coverage. Kubo *et al.* [61] did not reject the possibility of 1/2 ML as saturation coverage for 2×2 surface, either. Cho *et al.* [63] have performed high resolution core-level photoelectron spectroscopy for 2×2 and 2×3 structures. They did not find any difference in the behavior of Mg adsorption on Si(001) surface for these two configurations. They have found that the most preferable adsorption site for both of these low coverages is the cave site between two dimers (bridge site, in their notation).

On the theory side, Khoo and Ong [64] using a semiempirical self-consistent molecular orbital method have performed CNDO (complete neglect of differential overlap) calculations to investigate the adsorption of Mg atom on Si(001) at 1/2 ML coverage. According to their results the Mg atom resides on the bridge site above the midpoint of Si dimer.

Wang *et al.* [67], have done first principle calculations for the adsorption of another group II element Ba on Si(001) at a rather low coverage of 1/16 ML, and they have shown that the minimum energy site is the hollow site (cave-bridge site, in their notation) where the Ba atom is surrounded by four buckled dimers leading to a solitonlike defect in the original $c(4 \times 2)$ configuration.

The aim of this work [68] is to perform first-principle calculations for different coverages, i.e., 1/4, 1/2 and 1 ML, of Mg on Si(001) to get a clear understanding of

the adsorption mechanisms and to investigate the atomic structure of the surface covered with magnesium. To the best of our knowledge this is the first detailed work to investigate theoretically the Mg/Si(001) system for different coverages from first principles.

III.1 Method

We used pseudopotential method based on density functional theory in the local density approximation. The self consistent norm conserving pseudopotentials are generated by using the Hammann scheme [33] which is included in the fhi98PP package [31]. Plane waves are used as a basis set for the electronic wave functions. In order to solve the Kohn-Sham equations, conjugate gradients minimization method [38] is employed as implemented by the ABINIT code [69, 70]. The exchange-correlation effects are taken into account within the Perdew-Wang scheme [20] as parameterized by Ceperley and Alder [18].

The unit cell included an atomic slab with 8 layers of Si plus a vacuum region equal to about 9 Å in thickness. Each Si atom at the back surface is saturated with two hydrogen atoms in order to prevent the charge transfer between the surfaces. Single-particle wave functions were expanded using a plane wave basis up to a kinetic energy cut-off equal to 16 Ry. The integration in the Brillioun zone was performed using 8 special $\vec{k}$-points sampled using Monkhorst-Pack [26] scheme. Although a couple of cases were repeated with 18 special $\vec{k}$-points, no significant improvement has been observed.

We have used our theoretical equilibrium lattice constant for the bulk Si (5.405

Å) in the surface calculations. The bulk modulus for Si is found to be 96 GPa in rather good agreement with the experimental result of 98 GPa [71]. Our results for Mg bulk lattice parameter being 3.12 Å, and the c/a ratio being 0.607, obtained using 76 special $\vec{k}$-points, are very close to the experimental results of 3.20 Å and c/a of 0.614, respectively. As another check for our pseudopotentials, the lattice parameter for Mg_2Si was calculated to be 6.28 Å which is also in close agreement with the experimental value of 6.39 Å [72]. The energy bands of this compound gives a semiconducting gap of E_g equal to 0.14 eV. These tests suggest that the inclusion of the nonlinear core corrections to Mg pseudopotential is not needed.

We have used the 2×2 surface unit cell in our calculations to study the adsorption of Mg at a low coverage such as 1/4 ML and to include various combinations of adsorption sites for the half- and full-monolayer coverages. The first step was to optimize the clean Si(001)-2×2 surface while keeping the two lowest substrate layers (out of 8) frozen into their bulk positions and all the remaining substrate atoms and the hydrogen atoms were allowed to relax into their minimum energy positions. The $p(2\times2)$ was found to have the lowest total energy with a dimer length of 2.32 Å and a tilt angle of 19° which is in good agreement with the experimental dimer-length values of 2.40 ± 0.10 Å [73] and 2.20 ± 0.05 Å [74].

III.2 Results and Discussion

We have studied the adsorption of Mg atom on the Si(001) surface for 1/4, 1/2 and 1 ML starting with the reconstructed $p(2\times2)$ surface unit cell. We have chosen five

different sites for adsorption, namely, cave, hallow, pedestal, bridge and shallow. The cave site (c) is located above the fourth layer Si, hallow (h) and pedestal (p) sites are above the third layer Si, shallow site (s) above the second layer Si between two Si dimers, and the bridge site (b) is located above the dimer as indicated in Figure III.2. Note that in the figures 1 through 4 we have not shown the whole slab but depicted only a few layers from the surface for the sake of clearness. The adatom and the upper three monolayers of the substrate were then relaxed to their minimum energy configurations by performing structural optimization using the Broyden-Fletcher-Goldfarb-Shanno method [75] until the force on each atom reduces to a value less than 25 meV/Å. All of the calculations were done without any symmetry restrictions. Relaxation of more number of layers did not improve neither the energy values nor the atomic positions significantly.
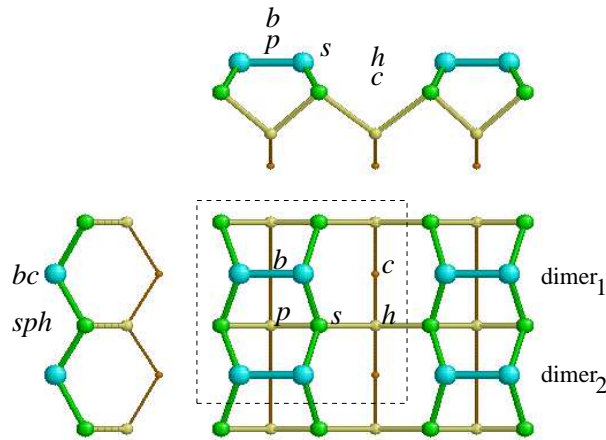
Figure III.1: Schematics of the adsorption sites for Mg atom on Si(001) surface from three different views. The symbols stand for: b=bridge, p=pedestal, h=hallow, s=shallow and c=cave. (The dimers are shown symmetric here for visual convenience)

In Table III.1 we introduce the structural parameters and bond lengths for different adsorption sites as well as the adsorption energy per adatom E_{ad} (negative of the binding energy of the adatom) given by

$$nE_{ad} = (E_{\mathrm{Si(001)}} + nE_{\mathrm{Mg}}) - E_{\mathrm{Mg/Si(001)}} \qquad \text{(III.1)}$$

where $E_{\mathrm{Mg/Si(001)}}$ is the total energy of the covered surface, $E_{\mathrm{Si(001)}}$ the total energy of clean surface, n is the number of Mg adatoms in the surface unit cell and E_{Mg} is the total energy of a single Mg atom with spin polarization obtained in a separate *ab initio* calculation using the same pseudopotential and the same energy cut off in a larger unit cell with a size of about 15 Å.

III.2.1   1/4 ML Coverage

(a)   (b)
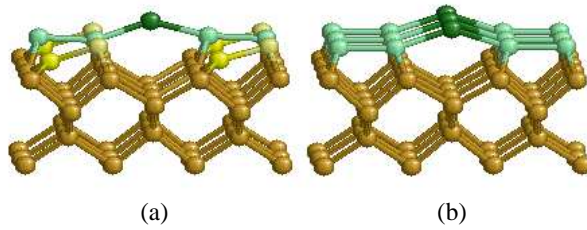
Figure III.2: Mg overlayer adsorbed on Si(001) surface (a) for 1/4 ML coverage on *c* site and (b) for 1/2 ML coverage on *c-c* site

The adsorption of Mg atom on cave site was found to be the most favorable one among the five different adsorption sites, shown in Figure III.2. The other cases, namely, the *s* site and the *b* site occupations by an adatom are also stable. However, in the case of adsorption of Mg on *p* or *h* sites, they migrate to different sites with lower energies. In fact, the adatom on *p* site migrates to the *s* site,

while the adatom on h site migrates to the neighboring c site. The adsorption of Mg on c site corresponds to an adsorption energy of 2.26 eV and s and b sites were found to be lower than that of c case by 0.25 eV and 0.68 eV, respectively. A natural pathway for surface diffusion might be $b \rightarrow s \rightarrow c$ in addition to $h \rightarrow c$ and $p \rightarrow s$.

For all stable cases in 1/4 ML coverage we have found that the surface dimers get partially symmetrized. Only one dimer ("dimer$_1$" to which Mg adatom bonds) becomes symmetric (with a tilt angle less than $\sim 6°$), while the other one ("dimer$_2$" with no charge transfer from Mg adatom) is still tilted (e.g., Figure III.2.1 a). The tilting angles for "dimer$_2$" in c, b and s cases being 16.0°, 17.1° and 13.0°, respectively, are still close to the clean surface value of 19° while "dimer$_1$" for all of them are almost flat as seen from Table III.1.

The height of Mg atom on cave site is found to be 0.75 Å which is in good agreement with the STM results of Hutchison *et al.* [60]. Figure III.2.1 a shows for the 1/4 ML coverage that the two Si atoms bonded to the same Mg adatom are still in an asymmetric environment. The one whose neighbors are tilted down is 2.68 Å away from Mg atom whereas the other has a bondlength of 2.65 Å. In a different calculation for Mg$_2$Si we have found Mg-Si bondlength to be 2.70 Å which is close to the back-bond lengths of Mg in this environment.

Table III.1: The structural parameters (in Å) for most of the stable adsorption sites for three different coverages Θ. The heights of the adatom with respect to the dimers (d$_\perp$ in Å) and the adsorption energies (E$_{ad}$ in eV) for these adsorption cases are also presented.

Θ	Model	dimer$_1$	dimer$_2$	d$_{Mg-Si1}$	d$_{Mg-Si2}$	d$_{\perp 1}$	d$_{\perp 2}$	2 × n	E$_{ad}$
1/4	c	2.54	2.28	2.68	2.65	0.75		2×2	2.26
	s	2.46	2.35	2.57	2.51	1.46		2×2	2.01
	b	2.51	2.29	2.54	2.49	2.08		2×2	1.58
1/2	c-c	2.54		2.68		0.82		2×1	2.20
	s-s	2.43		2.59		1.52		2×2	2.19
	s-s'	2.44		2.55		1.54		2×2	2.14
	p-h	2.87	2.91	2.66	2.93	1.32	0.57	2×2	2.01
	p-p	2.52		2.68		1.39		2×1	1.75
	b-b	2.55		2.53		2.18		2×1	1.52
1	s-s-s-s	2.38		2.73		1.49		2×1	1.98
	c-c-s-s	2.45		2.75	2.79	0.81	2.00	2×2	1.93
	p-p-h-h	–		2.65	2.87	0.53		(2)×1	1.91
	c-c-p-p	2.50		2.65	2.76	0.60	1.56	2×1	1.74
	c-c-b-b	2.58		2.59	2.69	0.59	2.36	2×1	1.59
	p-p-b-b	2.56		2.65	3.59	1.31	3.35	2×1	1.46

III.2.2   1/2 ML Coverage

For the case of 1/2 ML coverage, (i.e., 2 Mg atoms per 2×2 unit cell), we have considered the adsorption at combinations of pairs of the five different sites resulting in 15 different cases among which the most favorable case was found to be the *c-c* sites in our calculations. The structure then possesses 2×1 reconstruction with symmetric dimers stretched to 2.54 Å, shown in Figure III.2.1 b.

Even though *s* was stable for the low 1/4 ML coverage, we found that *s-s* is not always stable for 1/2 ML coverage. Out of four *s* sites in a 2×2 surface unit cell there are three inequivalent *s-s* geometries as shown in Figure III.2.2. For instance, it is unstable if the other adatom occupies the next *s* site along the [110], i.e., dimer row direction, as shown in Figure III.2.2 c. However, if the second adatom were added on the other *s* site along [$\bar{1}$10], i.e., the direction of dimers, as seen in Figure III.2.2 a, this 2×2 configuration will be stable and it will have an adsorption energy almost equal to that of the *c-c* case, differing by only 0.01 eV per adatom. The last case *s-s′*, with the second *s* site is along the [010] direction as shown in Figure III.2.2 b, is also stable with an adsorption energy of 2.14 eV per adatom.

Although neither of *p* and *h* sites are stable at 1/4 ML coverage, combination of them at 1/2 ML coverage, i.e., the *p-h* case with one atom occupying a pedestal site while the other occupying the neighboring *h* site was found to be stable and it is more favorable than the occupation of *p-p* sites that is also stable. In the case of *p-p* adsorption the adsorbed atoms are four-fold coordinated with the
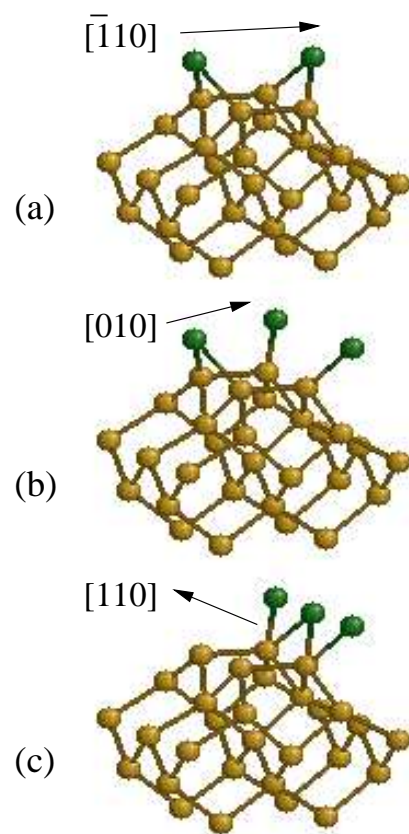
Figure III.3: Adsorption of two Mg atoms on *s* sites for half coverage: (a) *s*-*s* stable, (b) *s*-*s'* stable and (c) *s*-*s''* unstable configurations.

neighboring Si dimer atoms with a bond length of 2.68 Å and with symmetrical dimers stretched to a length of 2.52 Å. The case of adsorption on b-b was also found to be stable with symmetrical dimers but with an adsorption energy less than the c-c case by 0.68 eV per adatom.

The other combinations were found to be not stable and the adatom migrates to any one of the above stable configuration sites.

In all of the above stable configurations we have found that the surface dimers become symmetric (e.g., Figure III.2.1 b) in contrast to the 1/4 ML adsorption case discussed before. The dimer lengths for all the stable adsorption sites are in the range 2.43–2.55 Å except for the case of p-h adsorption where the two dimers were stretched to rather long values of 2.87 and 2.91 Å, respectively. This asymmetry makes it slightly a 2×2 rather than a 2×1 like most other cases in 1/2 ML coverage with the exception of the s-s case which is naturally a 2×2. As to the Mg–Si backbonds, they are in the range of 2.53–2.93 Å. In Table III.1 the d_{Mg-Si} values listed for the p-h case are for the Mg atom on p and h sites bonded to dimer Si atoms, respectively. Similarly, the $d_\perp$ values correspond to the heights measured from Si dimers of Mg adatoms on p and h sites, respectively.

In addition to the pathway $b \rightarrow s \rightarrow c$, we have also $b \rightarrow p \rightarrow s \leftrightarrow h \leftrightarrow c$ pathway in 1/2 ML coverage, where the backward migrations in energy take place among sites in the trough. Another rule brought by the double occupancy in this coverage is that the adatoms form chains along the dimer rows or along the dimer bonds. The s-s'-case looks like an exception to this, however, it is not considered to be a chain to first order. Any possible unstable combination α-β phase will

diffuse into one of the stable phases listed in Table III.1 by the adatom on either one of α or β sites migrating to a new site according to the above rules. In the case of b-c phase, since each Si atom of all dimers are bonded to two Mg atoms it is not stable and consequently, both Mg atoms at b and c sites migrate to their corresponding neighbors p and h sites, respectively, to reach the stable p-h phase. We should emphasize here that this conclusion is not only based on the total energy calculations but also on the comparisons of the Hellman-Feynman forces and the adatom behavior in the other less stable cases.

III.2.3 1 ML Coverage

For the full coverage adsorption, we have found six most probable configurations that are also consistent with our findings for the half coverage case. They are listed in Table III.1 in the order of their adsorption energies.

The adsorption on s-s-s-s was found to be the most favorable one with an adsorption energy of 1.98 eV per adatom. In this model we have four Mg atoms occupying all four s sites forming Mg lines that run along the dimer rows. The surface symmetry of this structure is 2×1 with dimers shortened to 2.38 Å as compared to 2.43 Å of the s-s half coverage case. Such a short dimer length may be due to the shortest Mg-Mg distance along $[\bar{1}10]$ obtained in the present case than in all the other geometries considered. The Mg-Si backbond of length 2.73 Å compares well with the Mg-Si bond (of length 2.70 Å) in Mg_2Si.

The next stable case that has less adsorption energy (by only 0.05 eV per adatom) is the c-c-s-s in which one has two Mg adatoms on s-s along the $[\bar{1}10]$

direction, while the other two Mg adatoms occupy the *c-c* sites along the [110] direction as seen in Figure III.2.3 b. In this case the reconstructed surface structure possesses a 2×2 symmetry with dimers of length 2.45 Å. The Mg-Si backbonds being in the range of 2.75–2.79 Å also compare well with the Mg-Si bonds in silicates.

The *p-p-h-h* combination, in which every hallow and pedestal sites are occupied, was also found to be stable with an adsorption energy differing from the *s-s-s-s* case by 0.07 eV per adatom. This phase is very interesting in its symmetry properties. Upon relaxation the dimers are removed and it approached to an almost 1×1 phase where *p* and *h* become the same. The deviation from 1×1 is very small and is due to a slight shift (0.15 Å) of only the ex-dimer-member Si atoms in the [$\bar{1}$10] direction opposite to one another, so that the Mg adatom will only bond to two Si atoms instead of four. This symmetry breaking due to charge transfer from Mg to surface Si atoms causes the zigzag bond picture shown in Figure III.2.3 c.

Next combination is the *c-c-p-p* case where the adsorbed atom in *p* site is four-fold coordinated with the neighboring Si dimer atoms with a bond length of 2.65 Å while the other adatom in cave site is two-fold coordinated with a bond length of 2.76 Å giving rise to an adsorption energy of 1.74 eV per adatom. This structure possesses 2×1 symmetry with a dimer length of 2.50 Å.

The combination *c-c-b-b* was also found stable with adsorption energy equal to 1.59 eV per adatom. In this model we have Mg atoms occupying all the bridge and cave sites, forming Mg lines that run orthogonal to the dimer rows
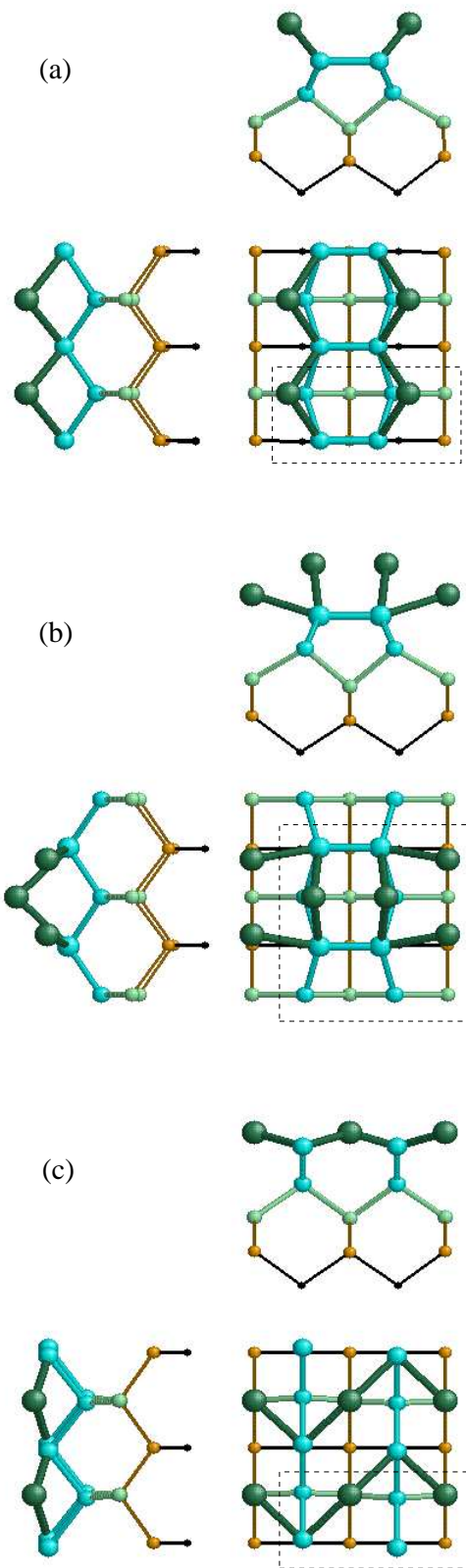
Figure III.4: Minimum energy structures for (a) *s-s-s-s*, (b) *c-c-s-s* and (c) *p-p-h-h* cases for 1 ML coverage.

and resulting in a 2×1 symmetry. The dimer length was found to be 2.58 Å. The difference in heights of the Mg adatoms on c and b sites measured from the silicon dimers corresponding to 1.77 Å undulates the Mg chains along the dimer direction.

The configuration p-p-b-b can be described as double half monolayer where two Mg atoms occupy two pedestal sites ($d_\perp$=1.31 Å) while the other two Mg adatoms rise further up to a height of 3.35 Å measured from the center of the dimer. This structure possesses 2×1 symmetry with a dimer length of 2.56 Å and can be described as undulated Mg wires located on the Si dimer rows, similar but orthogonal to the c-c-b-b case.

III.3   Thermodynamic Stability of the Phases

The thermodynamic stability for these coverages can be studied by calculating the grand canonical potential as a function of chemical potential for each case. This allows one to compare the stability of surface having different number of Mg adatoms.

The relative grand canonical potential [76] at 0 K can be written as

$$\Omega_{rel} = E - E_{clean} - n_{Mg}\mu_{Mg} \qquad \text{(III.2)}$$

where n_{Mg} is the number of adatoms and μ_{Mg} is the chemical potential of them, E and E_{clean} are the total energies obtained by the *ab initio* calculations for the covered and clean surfaces, respectively. The surface chemical potential μ_{Mg} of Mg should be considered in some range such that it cannot exceed the $\mu_{\text{Mg}}^{\text{bulk}}$. The
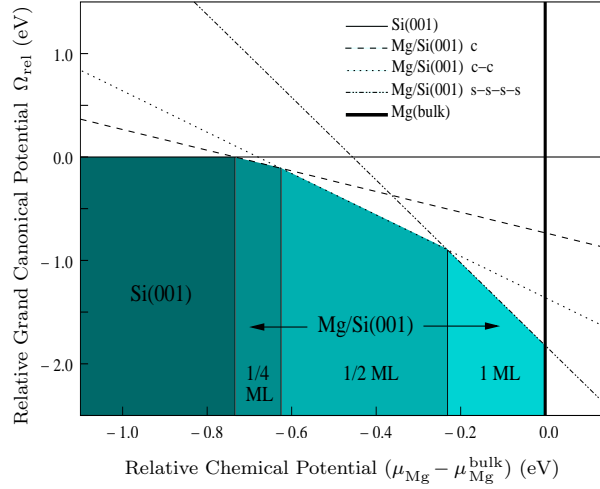
Figure III.5: The relative grand canonical potential as a function of the relative chemical potential of Mg adsorbed on Si(001) surface for the minimum energy cases of various coverages.

value of $\mu_{\mathrm{Mg}}^{\mathrm{bulk}}$ was obtained from a separate *ab initio* calculation for Mg in its crystal phase as described in Sec. II. Since the number of Si atoms is constant in all calculations, the relative grand canonical potential according to Equation III.2 is expected to vary linearly with Mg chemical potential for each coverage.

We have performed the calculations for 0, 1/4, 1/2, and 1 ML adsorption coverages with $p(2\times2)$, 2×2, 2×1, and 2×1 reconstructions, respectively. These reconstructions represent the most stable adsorption configurations for each coverage, i.e., *c*, *c-c* and *s-s-s-s*. The relative grand canonical potential Ω_{rel} as a function of $\mu_{\mathrm{Mg}} - \mu_{\mathrm{Mg}}^{\mathrm{bulk}}$ has been calculated and presented in Figure III.3. It was found that for $\mu_{\mathrm{Mg}} - \mu_{\mathrm{Mg}}^{\mathrm{bulk}} < -0.73$ eV the clean Si(001) surface has a lower energy than that with any amount of Mg adsorbed on it. However, in the range -0.73 eV $< \mu_{\mathrm{Mg}} - \mu_{\mathrm{Mg}}^{\mathrm{bulk}} < -0.63$ eV, the quarter coverage adsorption with a 2×2 symmetry is found to be the most stable structure. A transition to half

coverage with 2×1 surface has occurred when $\mu_{\mathrm{Mg}} - \mu_{\mathrm{Mg}}^{\mathrm{bulk}} > -0.63$ eV. Finally, when $\mu_{\mathrm{Mg}} - \mu_{\mathrm{Mg}}^{\mathrm{bulk}} > -0.23$ eV the full coverage occupation of the surface having the least energy is reached as explained in the *s-s-s-s* case. These findings suggest that all coverages that have been studied in the present work can be stable within the allowed chemical potential values of Mg.

III.4   Surface Energy Bands

In the following figures we present the calculated surface energy bands for the lowest energy structures projected on the bulk 2x2 unit cell. The projected bulk energy bands were also calculated using the same cutoff energy and lattice parameter.

In Figure III.6, we show our calculated band structure for the clean $p(2 \times 2)$ Si(001) surface. Our calculation which is in agreement with the other theoretical results reveals a semiconducting structure with a small gap due to the underestimation of the LDA approximation.

In Figure III.7 a, the energy bands of the lowest energy configuration of quarter coverage which corresponds to adsorption on c site are shown. The band structure shows a semiconducting surface with an indirect energy gap at $\Gamma - J$ equals to $0.187\ eV$.

In the cases of half coverage adsorption, Figure III.7 b, the calculated band structure of the lowest energy case *c-c* is also semiconducting with indirect band gap at Γ and a point along the line $J - K$ which is equal to $0.051\ eV$.

In Figure III.8, the adsorption of full coverage case, *ssss* is characterized by a
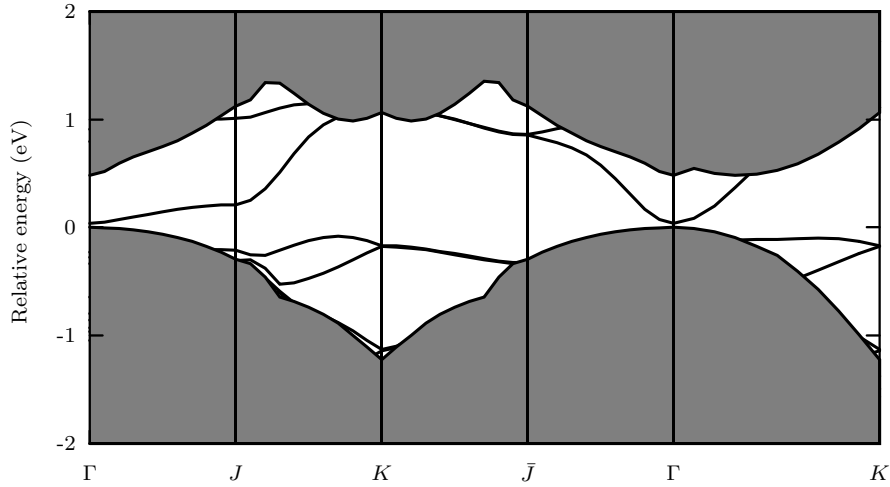
Figure III.6: Electronic band structure of the Si(001) $p(2 \times 2)$ surface. Projected bulk spectrum is shown by shaded region.

semiconducting band structure, in which we have an indirect band gap at Γ and a point along the line $J - K$ which is equal to $0.129 \ eV$.

III.5   Summary and Discussion

We have performed an *ab initio* total energy calculation and geometry optimization for a clean Si(001) surface and that with Mg overlayer of different coverages on it. For the 1/4 ML coverage we have found two favorable adsorption sites, namely c and s with a relative adsorption energy difference of only 0.25 eV per adatom. Our results agree well with the room-temperature results of Hutchison *et al.* [60] and of Cho *et al.* [63] where they have suggested that the most favorable site is the cave site. Kubo *et al.* [61] have suggested for the higher temperature adsorption that the s site is favorable, however, they assumed an extra Si on the surface bonding to the adatom. Even though Kubo et al. [61] suggested the
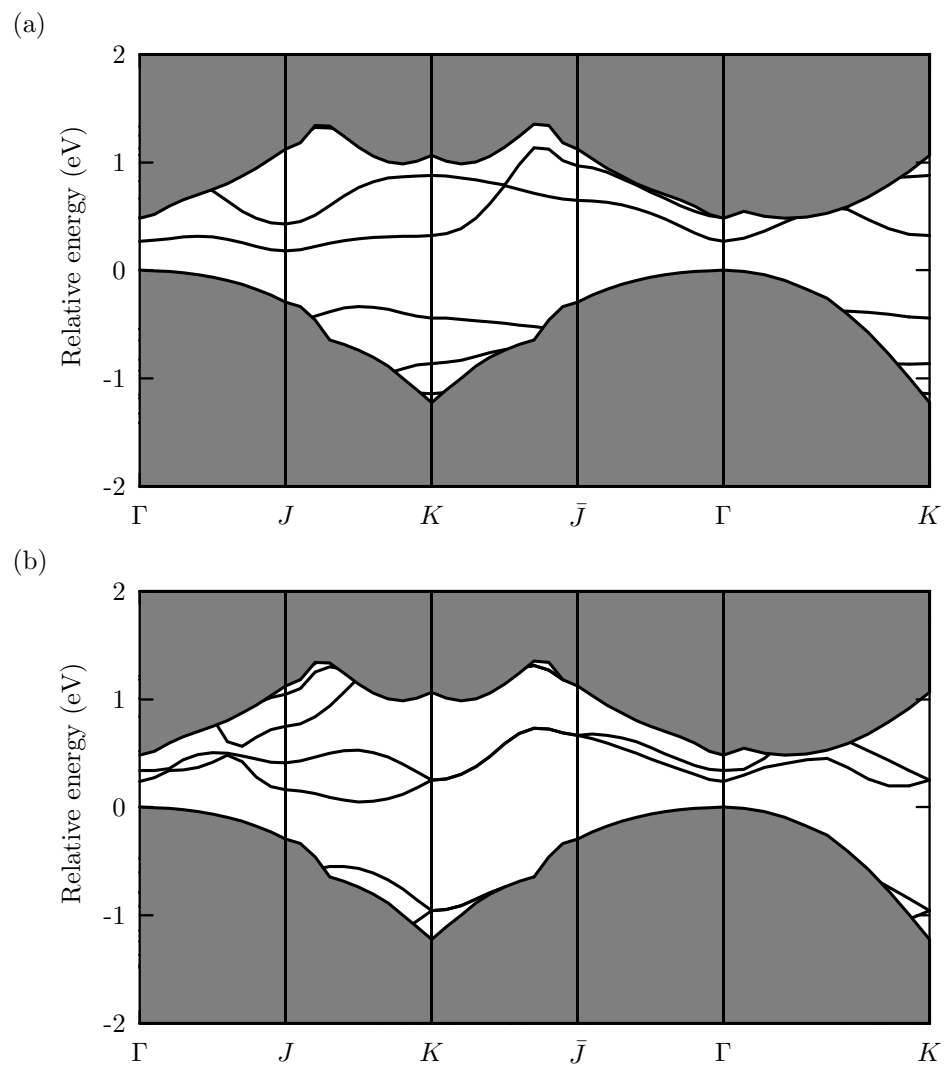
Figure III.7: Electronic band structure of (a) c (b) cc adsorption cases. Projected bulk spectrum is shown by shaded region.
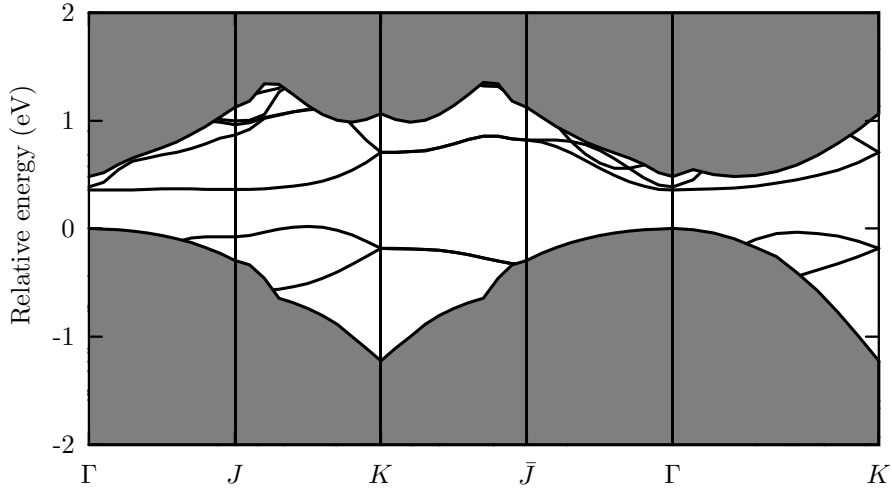
Figure III.8: Electronic band structure of the *ssss* adsorption case. Projected bulk spectrum is shown by shaded region.

possibility of single adatom occupation on a pedestal site at room temperature, we did not find any evidence to confirm it. Our calculations show that this site is unstable for a single adatom adsorption. Occupation of pedestal site has also been ruled out by Cho *et al*. [63] for low coverage. But we find that the argument of Hutchison *et al*. [60] that this site can be occupied by multiple atoms is in agreement with our stable *p-p* case for 1/2 ML.

Contrary to the theoretical results [67] for Ba adsorption on Si(001), we found that the Mg adsorption on *h* site is not stable. Since the total energy of this case being higher than the adsorption on *c* site by 0.85 eV per adatom, it leaves this saddle point and migrates to the neighboring cave site. We believe the reason for this disagreement with the Ba case might be due to the difference in their atomic sizes.

For the case of half monolayer coverage, our results give 2×1 reconstruction

with the Mg adatoms on c-c sites. The high temperature result of Kubo et $al.$, [61] for the same coverage suggested that it contains two Mg adatoms located nearly on c-c sites but distorted by the existence of an extra Si atom which causes the symmetry to be a 2×2. On the other hand, their 1/2 ML result for low temperature can be described as two Mg adatoms confined in every other cave site and separated towards h-saddle to make it a 2×2. This corresponds to a distorted version of our h-h case. Starting from both of these geometries we have found them unstable ending up in c-c case with a 2×1 symmetry. Even though we have started with a 2×2 unit cell for each case, we have ended up with 2×1 reconstruction for the 1/2 ML coverage except for the s-s cases, which are naturally 2×2, and the p-h case which is a slightly 2×2 distorted from 2×1. This slight symmetry breaking shows up itself in 1 ML coverage case of p-p-h-h as well.

The bridge site b-b was found to be stable in accordance with the theoretical result of Khoo and Ong [64] for this coverage, even though it is the least favorable case.

For the case of full monolayer coverage, we have found that the adsorption model in which all the Mg atoms occupy all the s sites with 2×1 construction is more favorable than 2×2 reconstruction in which Mg atoms occupy two shallow and two cave sites having an adsorption energy difference of only 0.05 eV per adatom. The next favorable case having 0.07 eV per adatom smaller adsorption energy than the most preferable s-s-s-s case is the p-p-h-h configuration

63

with a 2×1 symmetry, but just slightly away from 1×1 geometry as seen in Figure III.2.3 c. This may suggest that more than 1 ML coverage might lead to a 1×1 phase consistent with the LEED results of Kim *et al.* [62] who reported that the 1×1 phase corresponds to 2 ML coverage.

The model of adsorption that can be concluded from our theoretical results is that for the low coverage, Mg atoms will be adsorbed mostly on c sites and less likely on s sites, which continues until the coverage reaches to 1/4 ML. As the coverage exceeds 1/4 ML, the Mg atoms are adsorbed on the c-c sites and on the s-s sites along $[\bar{1}10]$ with almost equal probabilities until the surface becomes saturated at 1/2 ML, where it is going to have domains of c-c and s-s phases with 2×1 and 2×2 reconstructions, respectively. Further increase in coverage will result into s-s-s-s, c-c-s-s and even p-p-h-h domains with 2×1, 2×2 and almost 1×1 reconstructions, respectively.

Using *ab initio* total energy calculations we have performed detailed investigation of the atomic geometry of Mg adsorbed Si(001) surface for 1/4, 1/2 and full monolayer coverages. We have investigated the adsorption sites, the energetics and the reconstruction of Si(001) surface after Mg adsorption. We have found that our results agree well with the existing experimental observations.

CHAPTER IV

STABILITY OF Sb MONOLAYER ON Si(001) AND Ge(001) SURFACES

The adsorption of group V elements on surfaces of group IV elements has been the subject of great interest both theoretically and experimentally in the last few years. The interest has grown because of the influence of group V elements in enhancing the abruptness of the interface in crystal growth of heterostructures by acting as surfactants, and in modifying the electronic properties by acting as dopants [77-79]. The adsorption of As and Sb under good experimental conditions leads to a well ordered symmetric dimer structure on both Si(001) and Ge(001) surfaces. Although both As and Sb are characterized by similar dopant and surfactant behaviors, they do not necessarily exhibit similar structural pattern.

The As-covered Si(001) surface is observed to have less anti-domain phases and defects than the Sb-covered Si(001) surface [80-82]. This is believed to be

due to difference in surface stresses caused by the adsorption of these group V elements [99]. As covered surface has an isotropic stress being tensile in both directions, while it is anisotropic in Sb covered case [82], tensile in bond direction and compressive along dimer rows.

It is believed that the stress relief effects play very important roles in the reconstruction, antiphase domain boundary formation and defects that appear on Sb/Si(001) surface. One of the mechanisms that was suggested for stress relief is the displacive adsorption which has been introduced for the first time by Alerhand *et al.* [83] in order to solve the dimer orientation dilemma in As covered Si(001) system.

It was suggested that during the growth process at low coverages of As, some As dimers replace the Si dimers on top of the Si substrate in order to reduce the surface stress. In fact, in all displacive adsorption processes, the driving force for such phenomena was believed to be the reduction of either extrinsic (step related) [83] or intrinsic (terrace related) stress [84].

In a recent experimental work, Saranin *et al.* [85] have shown that the atomically flat Sb-terminated Si surface begins to get rough at a critical temperature of around 750°C, until which the surface remains flat. They have suggested that the displacive adsorption mechanism can lead to such phenomena, by assuming that some Sb atoms due to surface stress might diffuse into the substrate replacing silicon atoms, and pushing them to the surface instead. However, since energetically the Sb atoms prefer to reside at the top of the surface, they eventually diffuse out over the segregated Si atoms leading to surface roughening as a result.

Similar results have been obtained in a recent experimental work [86] where it has been shown that the highly ordered 1 ML Sb covered Ge surface is not stable. Instead the surfaces with anti-domain phases and low ordering are more stable. In their article it was proposed that this fact might be due to the anisotropy in surface stress.

The aim of this chapter is to study the 1 ML Sb/Si(001) and Sb/Ge(001). We will investigate the evolution of surface stress and its energetics as Sb atoms get interdiffused into deeper layers.

IV.1 Method

In this *ab initio* study, for either Si(001) or Ge(001) we considered an artificially constructed periodic geometry along the surface normal. The unit cell included an atomic slab with eight layers of substrate plus a vacuum region equivalent to about six substrate layers in thickness. The two back substrate layers were frozen into their bulk positions, and each atom at the back surface was saturated with two pseudo-hydrogen (H_{ps}) atoms. All the remaining substrate atoms, the adsorbate atoms and the saturating H_{ps} atoms were allowed to relax into their minimum energy positions. Single-particle wave functions were expanded using a plane wave basis up to a kinetic energy cut-off of 16 Ry.

For the surface stress calculations we have considered a symmetrical unit cell which included an atomic slab with 8 layers of Si (Ge) and one monolayer of Sb on each surface. The vacuum region between slabs was taken to be about 8 monolayer in thickness. All of the atoms were allowed to move except the two layers in the

middle of the slab. The integration in the Brillouin zone was performed using 8 special k points sampled within the Monkhorst-Pack scheme [26]. Even though the contribution to the surface stress comes mostly from the first 3 monolayers, we let also the deeper layers of the substrate to relax and we have found that 4 layers were enough for the purpose.

The surface stress was extracted from the three dimensional surface stress by the relation [87]

$$g_{\alpha\beta} = \frac{c}{2}\sigma_{\alpha\beta}^{\text{corr}} = \frac{c}{2}(\sigma_{\alpha\beta} + \chi\delta_{\alpha\beta}),$$

where c is the height of the supercell, χ is the finite basis correction, and $\sigma_{\alpha\beta}$ is the 3-dimensional supercell stress tensor [88].

IV.2 (2×1) clean Si(001) Surface

For the surface calculations we have adopted our theoretical equilibrium lattice constant for the bulk Si (5.405 Å). We started by optimizing the clean surface of Si(001). We found that the dimers are tilted with an angle of 18.0° and the dimer length is about 2.27 Å.

Our result for clean Si(001) is in agreement with the theoretical results of Ramstad *et al.* [89] who found a dimer length of 2.26 Å with tilting angle being 18.3°. Our results also agree with the theoretical results of Krüger *et al.* [79] who found using gaussian orbital pseudopotential calculations a dimer length of 2.25 Å and angle of 19°.

Table IV.1: Calculated dimer lengths and backbond lengths for the Sb/Si(001)-(2×1) surface in comparison with other experimental and theoretical results, for the geometry a depicted in Figure. IV.1

	Sb-dimer (Å)	Sb-Si backbond (Å)
Present work	2.94	2.56
Experiment [90]	2.88	2.63
Theory [91]	2.93	2.61
Theory [92]	2.94	2.59

IV.3   As and Sb Covered Si(001) Surface

As an initial step we started by studying the As terminated Si(001) surface. Our results show a symmetric dimer with the dimer length equal to 2.52 Å, and the backbond length of 2.42 Å. In the case of Sb adsorption on Si(001) we still have symmetric dimers but with lengths equal to 2.94 Å and backbonds of lengths 2.59 Å. Our results are in agreement with the the other theoretical and experimental results as shown in Table IV.3.

Our calculated surface stress for As is isotropic as expected, being tensile in both directions, with a relative anisotropy of 0.15 eV per (1×1) unit cell in agreement with the previous theoretical results [93, 94, 95]. In the case of Sb/Si(001) our calculated surface stress is anisotropic in both directions, being compressive parallel to the dimer rows and tensile in the orthogonal direction with a relative anisotropy of 3.07 eV per (1×1) unit cell.

Since the nature of stress of covered surfaces depends strongly on the size of the adsorbate atom and the chemical properties of the adsorbate, the difference

in stress behavior of both cases might be due to the difference in relative atomic sizes of As and Sb, while As has nearly the same size as silicon, Sb is 40% larger.

IV.4   Sb Interdiffusion in Si(001)

In this work we have considered that Sb atoms interdiffuse into Si substrate as seen in Figure IV.1, and have calculated the minimum energy configurations for various phases of such interdiffusion. In Figure IV.1, the labels (a), (b), (c), and (d) indicate four different configurations for Sb atoms on the surface, schematically. The geometry labelled (a) corresponds to non-diffused configuration, and the geometries labelled (b) and (c) correspond to 50% interdiffusion of Sb into the second and third substrate layers, respectively. We have also considered the possibility of two Sb atoms per (2×1) cell occupying the second layer while the Si atoms float to the surface (i.e., 100% interdiffusion of Sb into the second substrate layer), namely configuration (d). From our total energy calculations, it is observed that the system becomes energetically unfavorable as the amount of Sb-interdiffusion increases. The relative energies of the geometries (a), (b), (c) and (d) are found to be 0.0, 1.21, 1.72, and 2.62 eV per (2×1) unit cell, respectively. It can be concluded that as the degree of Sb-interdiffusion increases, the structure becomes energetically less favorable. The energetic favorability of the Sb-on-top structure can be explained by using simple physical arguments based upon different bond strengths among group IV and group V atoms (Si-Si: the strongest corresponding to shorter bond lengths; Si-Sb: intermediate; and Sb-Sb: the weakest) [96]. In Table IV.4, we have tabulated all the structural
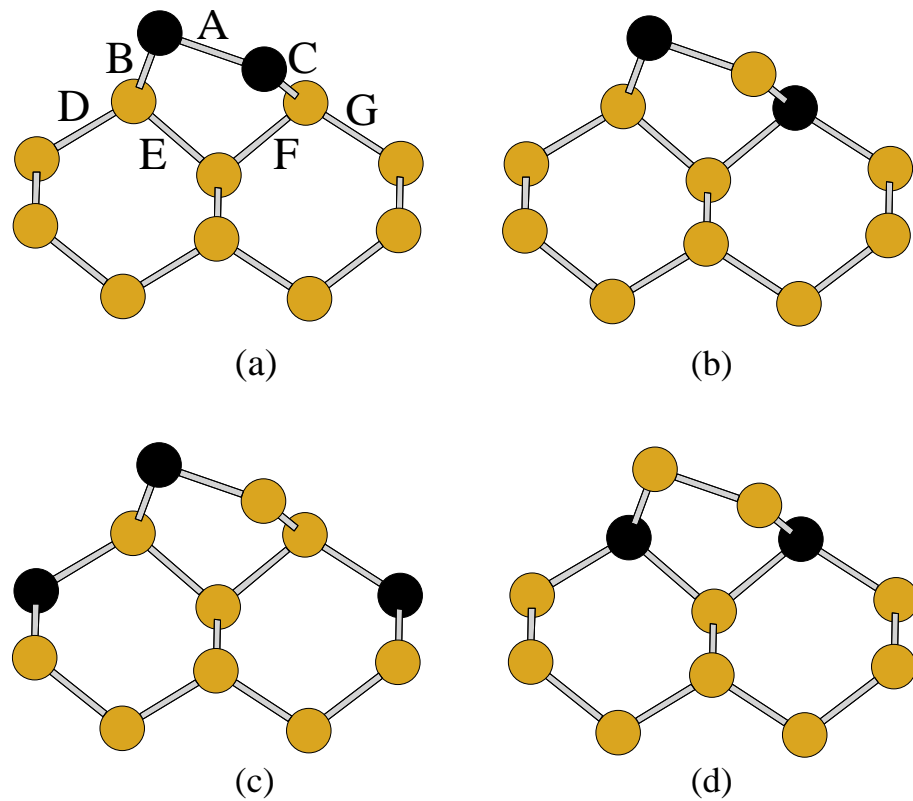
Figure IV.1: Schematic views of atomic arrangements for the 1 ML of Sb atoms adsorbed on the X(001), X = Si, Ge : (a) Sb-capped X(001)-(2×1), (b) 2nd layer Sb-interdiffused X(001)-(2×1), (c) 3rd layer Sb-interdiffused X(001)-(2×1), and (d) X-capped (Sb-segregated) X(001)-(2×1). The dark filled and light filled circles represent Sb and X atoms, respectively.

Table IV.2: Key structural parameters, in Å, and the relative energies (ΔE) of Sb/Si(001) and Sb interdiffusion configurations indicated in Figure IV.1 (a) to (d).

Geometry	A	B	C	D	E	F	G	ΔE (eV)
Sb-capped (a)	2.94	2.56	2.56	2.36	2.31	2.30	2.30	0.00
2nd layer (b)	2.75	2.60	2.55	2.33	2.29	2.53	2.59	1.36
3rd layer (c)	2.72	2.55	2.36	2.57	2.30	2.31	2.59	1.90
Si-capped (d)	2.49	2.58	2.58	2.57	2.53	2.53	2.57	2.72

parameters and the relative energies . The bond lengths vary between the values 2.29-2.49 Å for the Si-Si, 2.51-2.75 Å for the Si-Sb, and 2.92-2.94 Å for the Sb-Sb bonds in various environments, described by the geometries (a) to (d), consistent with the bond strengths.

Since our calculations based on infinitely repeated dimers were made at zero temperature, by using our total energy results that neglect thermal effects, we can only estimate an interpolation of Sb interdiffusion to higher temperatures. The relative energy results for the four configurations presented allow us to employ a Boltzmann analysis to estimate layer occupation probabilities for the Sb adatoms. The procedure we have followed has previously been established [97, 98]. Examining the Boltzmann probability distribution for the above four configurations, we found that the interdiffusion is unlikely to happen even for temperatures as high as 750°C as the probability is too small.

For surfcae stress calculations, when we had one atom of the Sb-Sb dimer bond get adsorbed into the second layer we found that a very strong relief in the

tensile stress along the dimer bond took place, with a relatively smaller increase in the compressive stress normal to the dimer, resulting in a more isotropic stress of 2.03 eV per (1×1) unit cell.

When the surface is totally covered by Si on top of Sb (geometry (d)) the surface gets compressive in both directions with an anisotropy of 1.08 eV per (1×1) unit cell indicating a reduction in surface stress anisotropy. Our stress and energy calculations that it is not favorable for Sb atoms to get adsorbed into the bulk, but the reduction of the surface stress may drive the atoms to do so. As the atoms get adsorbed as a result of stress relief, and segregation of Si atoms on top of Sb starts takes place, the reduction of energy will further lead the Sb atoms to diffuse over Si, but with less order, resulting in surface defects with which the surface must have less stress anisotropy and less energy as long as all Sb atoms will lie finally on the top of Si atoms.

Finally, for As/Si(001) surfaces, our calculation stated that it is not preferable for As/Si(001) to lie below Si layer since it is not favorable neither from energetic point of view, nor from that of stress. Adsorption of As into the first layer will increase the energy and will lead to strong anisotropy in stress which our calculation shows that it is equal to 1.15 eV per (1×1) unit cell. This may explain reason beyond the existence of defects and roughness on Sb/Si(001) surface and not on As/Si(001). This conclusion is in agreement with the recent theoretical work of He et al. [99], who have employed a tight binding molecular dynamics to investigate the surface stress evolution as defects appear on the Sb/Si(001) surface. Their results have shown that introducing defects on the surface results

Table IV.3: Calculated dimer lengths and backbond lengths for the Sb/Ge(001)-(2×1) surface in comparison with other experimental and theoretical results, for the geometry *a* depicted in Figure IV.1.

	Sb-dimer (Å)	Sb-Ge backbond (Å)
Present work	2.94	2.62
Experiment [100]	2.90	2.47, 2.49
Theory [101]	2.95	2.62
Theory [102]	2.92	2.59

in a significant relief of the compressive contribution to the stress along the dimer row and thus a decrease of the stress anisotropy.

IV.5 Clean Ge(001) Surface

For the surface calculations we have adopted our theoretical equilibrium lattice constant, 5.58 Å, for the bulk Ge. We started by optimizing the clean Ge(001)-(2×1) surface. We found that the dimers are tilted with an angle of 18.3° and the dimer length is about 2.42 Å.

IV.6 Sb Terminated Ge(001) Surface

The calculated Sb-Sb dimer length of 2.94 Å and the backbond Sb-Ge length of 2.62 Å are in good agreement with the results of other theoretical calculations that are listed in Table IV.6.

IV.7 Interdiffusion of Sb into Ge(001) Surface

We have also tabulated all the structural parameters and the relative energies Table 2. The bond lengths vary between the values 2.38 – 2.64 Å for the Ge-Ge, 2.58 – 2.81 Å for the Ge-Sb, and 2.94 Å for the Sb-Sb bonds in various environments, described by the geometries (a) to (d) in Figure IV.1, consistent with the corresponding bond strengths. The dimer tilt angles for these geometries (a) to (d) were found to be 0, 4.9, 0.7 and 0°, respectively. The Sb-capped (i.e., Sb-on-top structure) Ge(001)-(2×1) surface structure was found to correspond to the lowest energy configuration. The overall energetic trend is similar to that for the Sb-adsorbed Si(001) surface, and can be explained by using simple physical arguments based upon different bond strengths among group IV and group V atoms (Ge–Ge: the strongest corresponding to shorter bond lengths; Ge–Sb: intermediate; and Sb–Sb: the weakest).

For Stress calculations, our results which are presented in Table IV.7, show that the lowest energy configuration in Figure IV.1 (a), the Sb-capped surface, is characterized by stress which is compressive along the surface dimer row direction and tensile in the orthogonal direction, with an anisotropy of 1.38 eV/(1×1) unit cell. Compared to our previous calculations for Sb/Si(001), it is obvious that Sb/Ge(001) is relatively more isotropic. We explain this in terms of a smaller difference in the relative sizes of Sb and Ge, versus that of Sb and Si: the Sb atom is 40 % bigger in size than Si atom, while it is only 16 % bigger than the Ge atom. Using this argument, the As/Si(001) exhibit an almost isotropic surface

Table IV.4: Key structural parameters, in Å, and the relative energies (ΔE) of Sb/Ge(001) and Sb interdiffusion configurations indicated in Figure IV.1(a) to (d).

Geometry	A	B	C	D	E	F	G	ΔE (eV)
Sb-capped (a)	2.94	2.62	2.62	2.45	2.38	2.38	2.45	0.00
2nd layer (b)	2.81	2.61	2.67	2.42	2.38	2.58	2.66	0.63
3rd layer (c)	2.80	2.61	2.47	2.64	2.39	2.41	2.66	1.12
Ge-capped (d)	2.64	2.65	2.65	2.63	2.58	2.58	2.63	1.47

stress behavior on account of similar atomic sizes of Si and As as stated before.

The total energies of the geometries with Sb adsorbates interdiffused into the second and third layers of Ge(001) [Figure IV.1 (b) and (c), respectively] are 0.63 eV and 1.12 eV higher than the energy of the Sb-capped geometry [Figure IV.1 (a)]. For these geometries the surface becomes less tensile in the direction of surface dimer bond and more compressive in the orthogonal direction. And more importantly, these geometries result in a decrease in the anisotropy in surface stress. A complete segregation of Ge atoms on the top of the Sb atomic layer [Figure IV.1 (d)] leads to an energy increase of 1.47 eV. For this situation the surface experiences compressive stress in both directions. However, there is a huge reduction in the stress anisotropy, to only 0.67 eV/(1×1) unit cell. We note that the total energy calculations resulted in dimers that are almost flat. The only dimer that is tilted is the Sb-Ge dimer in the second geometry [Figure IV.1 (b)] with a small tilt angle of merely 4.9°. Our estimate of an upper limit for the energy gain upon dimer tilt is 0.05 eV. Even this energy is a very small fraction

Table IV.5: Calculated surface stresses, in eV per (1×1) unit cell, for different structures, both for the directions parallel ($g_\parallel$) and perpendicular ($g_\perp$) to dimers, as well as the corresponding stress anisotropy ($g_\parallel$–$g_\perp$) for both Ge and Si case.

Sb/X(001)	X = Si [103]			X = Ge [104]		
	$g_\perp$	$g_\parallel$	$(g_\parallel$–$g_\perp)$	$g_\perp$	$g_\parallel$	$(g_\parallel$–$g_\perp)$
Sb-capped (a)	− 1.48	1.59	3.07	− 0.47	0.91	1.38
2nd layer (b)	− 1.65	0.38	2.03	− 0.64	0.42	1.06
3rd layer (c)	− 1.49	− 0.09	1.38	− 0.73	0.19	0.92
X-capped (d)	− 1.84	− 0.78	1.08	− 0.74	− 0.07	0.67

of the relative energies of the four configurations described above.

Examining the Boltzmann probability distribution for the above four configurations, we found that a very small number (only approximately 0.06 % of the surface Sb atoms) might diffuse into the second substrate layer. This is slightly different from the case of Sb on Si(001) surface, where we found that any adsorption of Sb atoms into the second substrate layer is almost impossible due to the high total energy difference [103].

As a result we have found that, similar to the case of Sb on Si(001), the Sb/Ge(01) surface is subject to a competition between stress relief by the adsorption of Sb into the Ge substrate layer and an energy gain by keeping the Sb on the surface. This dilemma can be resolved if we assume that Sb can in the first stage be adsorbed into the substrate, but due to the high energy difference it will diffuse back to the top of Ge in random positions, i.e., the final surface will not be highly ordered but will contain defects. Such a configuration will be more stable energy-wise and stress-wise.

CHAPTER V

SILICON THIN FILM GROWTH ON Si(001)

During the past decades thin films have been the subject of theoretical and experimental studies due to their technological importance in many fields as optical coating, corrosion protection and utility in semiconductor devices. They are also important within physical science itself in exploring differences between three-dimensional and (quasi-)two-dimensional states of matter such as the decrease in conductivity of thin metal films and the variation in thermodynamic properties, or chemical reactivity, as a function of film thickness. Often thin films are important in arrangements for experiments on other topics, such as absorbing x-rays or polarizing neutrons [105].

Thin films can be prepared in the laboratory using chemical vapor deposition (CVD), molecular beam epitaxy (MBE) or ion beam deposition (IBD). The ion beam deposition technique provides a way of depositing isotopically pure thin films and hetrostructures with ion incident energies that can be varied between

0-1000 eV, and the ions can be deposited without chemical limitations imposed by CVD techniques. It provides the ability to chose the incident ion energy and precisely control the dose rate which enables the growth parameters to be tailored towards a specific goal, such as low temperature epitaxial growth.

Silicon thin film growth has been of major interest in view of the desirability of reducing growth temperatures below those temperatures associated with MBE (600-850°C) [107], Miyakane et al [108] used IBD to grow Si(001) thin films using a 200 eV ion energy at room temperature and 740°C. Only the high temperature results produced crystalline films, whereas those obtained at room temperature were amorphous as observed by using RHEED.

Zalm et al [109] could produce epitaxial films of Si on Si(001) and Si(111) using 50 eV ion energy at 400 K for substrate temperature. The crystallinity of the films was monitored by RHEED and extreme sensitivity to the conditions of substrate prior to deposition was observed. Herbots *et al.*, [110] in their experimental work have studied the growth by using 20 and 40 eV ion energies with three different substrate temperatures, namely, 350, 400, and 600°C. They have observed epitaxial growth at all of the three temperatures. The different defect structures observed in the TEM micrographs however, were attributed to the different substrate temperatures.

Orrman-Rossiter *et al.* [111, 112] addressed also the dependence of thin film epitaxy on ion energy and substrate temperatures in their experimental work. They have shown that the crystalline quality of silicon films get enhanced monotonically as ion energy is decreased from 100 to 10 eV for substrate temperatures

79

$\geq 350°$C.

Matsuoka and Tohno [113] have shown that crystalline films of silicon can be grown at $320°$C for Si^+ ion energies ≤ 25 eV; on the other hand it was found that defect density increased drastically for energies above 50 eV. Albayati et al, [114, 115] have noticed also strong energy and temperature dependence of the crystal quality as they achieved the epitaxial growth at $290°$C using 15-eV Si^+.

Rabalais *et al.* [116] have investigated the ion beam deposition of Si at various ion incident energy and substrate temperatures, they have found that layer-by-layer growth has been observed down to $160°$C with appropriate ion energies. Below this temperature, island growth with transition to an amorphous phase occurs. They have found also an optimum ion-energy windows for achieving layer-by-layer epitaxial growth and high crystalline quality at substrate temperatures of $160°$C and $290°$C.

Another method of enhancing the epitaxial growth at low temperatures, is the ion beam assisted deposition, in which a second beam of inert gas or another material is allowed to strike the growing surface, which enhance the crystallinity of the material obtained [113-116].

Various molecular dynamics simulations has been reported in literature for the IBD system. Kaukonen *et al.* [121] have reported the molecular dynamics simulation of ion beam deposition of carbon on diamond. They have found that at room temperature there is a window 40-70 eV at which a diamond film can grow. Hensel *et al.* [122] using a classical molecular-dynamics simulation, have

studied the homoepitaxial growth on a Si(100)(2×1) surface at 300 K. they compared the structures resulting from the deposition of 2-eV Si atoms, and from a 2% admixture of 30-eV Si atoms. Energetic atom bombardment results in a considerably reduced amorphous layer.

In this work we will study the crystallization of deposited films as functions of substrate temperature and ion energy. We will perform the simulation at three typical values of substrate temperature, the extremely low temperature of (1K), intermediate (300K), and high temperature (1000K). At the same time we will investigate the effect of different incident ion energies 2, 10, 20, 40, and 70 eV. We will analyze the results on the basis of the radial distribution function, bonding angles, vertical film density, coordination number, and dihedral angles.

V.1 Method

In all MD simulations done in this work, reconstructed (001)-2×1 surfaces of silicon crystals with symmetric dimers were used as substrates, which were taken to be 9 ML thick. Each monolayer contains 4×4 matrix of atoms. By using the lateral periodic boundary conditions, we imitated an infinite crystalline slab for the substrates. The atoms at the bottom layer were held fixed. In all cases the substrate was initially thermalized at the chosen temperature for 40 ps, then during the growth simulation, the three layers immediately above the bottom layer are held fixed at the desired temperature by scaling the velocities at each time-step in order to simulate the heat bath. After thermalization, 128 new atoms corresponding to 8 ML are deposited, by having atoms impinging normal to the

surface one after another, allowing a time interval of 8 ps between successive ion bombardments. This will corresponds to a deposition rate equal to 5.26×10^{24} particle/cm^2. The lateral starting positions of the impinging atoms are chosen randomly but were identical in all simulations. After the deposition is completed, the slab is allowed to thermalize for a duration of 40 ps. Using the above procedure we simulated the crystal growth for Si on Si, in a manner similar to that of ion beam bombardment experiments.

V.2 Lattice Parameter vs. Temperature

In order to do simulation at finite temperature, one has to use the correct lattice parameter at that temperature. Using constant temperature and pressure algorithm we can allow the lattice volume to change, and hence the lattice parameter such as to minimize the stress.

The lattice parameter values as estimated by SW potential at different temperatures are shown in Table V.2.

V.3 Vertical Density

In Table V.3 - V.3 we present the particle density profile $\rho(h)$ of the grown film perpendicular to the substrate. Our data is given in units of surface density of (001) in silicon crystal. The density in the table is given at typical values of $\rho_n = \rho(L_n)$ where $n = 1, ..., 10$ denoting the hight index of grown monolayers.

We did not find considerable dependence of the film density profile for the first grown six monolayers on the energy of incident particle or the substrate

Table V.1: The corresponding lattice parameter for silicon as calculated by NPT molecular dynamics for SW potential

Temperature (K)	a (Å)
0	5.431
100	5.432
200	5.433
300	5.434
400	5.435
500	5.436
600	5.437
700	5.437
800	5.438
900	5.438
1000	5.439
1100	5.440
1200	5.440

temperature, however, some small dependence were observed in the higher grown monolayers as well as in the substrate monolayers.

In general we found three common features for all grown films: First, a small deviation around the ideal density value is found among the first grown six monolayers, which gets larger for higher monolayers. Second, we observed the existence of some atoms in higher layers as high as ninth or tenth layers in most of the grown films. Third we noticed that considerable diffusion into the substrate monolayers took place when incident particle energy $\geq$ 40 eV.

At 1 K growth temperature we found that the amount of diffused atoms into the substrate increased from 0.05 ML at 40 eV to 0.12 ML at 70 eV. For the growth at 300 K the amount of diffused atoms increased from 0.6 ML at 40 eV to 1.23 ML at 70 eV leading to an almost empty eighth layer in the later case. The same behavior was seen on higher temperature growth where diffusion increased

from 0.9 ML to 1.4 ML at 40 and 70 eV, respectively. As expected, the previous results suggest that using high energy incident kinetic energies ≥ 40 eV at higher substrate temperature ≥ 300 K, will lead to diffusion, as opposed to growing at very low temperatures where the amount of diffused atoms was very small.

Table V.2: Deviation of Bulk vertical density ρ in percentage for grown structures at 1 K with various incident kinetic energies averaged over 10 independent runs.

E(eV)	ρ_1	ρ_2	ρ_3	ρ_4	ρ_5	ρ_6	ρ_7	ρ_8	ρ_9	ρ_{10}
2	−1	3	1	5	0	7	−3	−29	15	1
10	−1	1	−2	7	−3	4	-9	−21	23	1
20	0	3	−4	3	3	−8	−8	−13	23	1
40	1	1	−1	0	−7	−2	−13	−8	24	0
70	1	2	−2	−2	−8	8	6	−24	8	0

Table V.3: Deviation of Bulk vertical density ρ in percentage for grown structures at 300 K with various incident kinetic energies averaged over 10 independent runs.

E(eV)	ρ_1	ρ_2	ρ_3	ρ_4	ρ_5	ρ_6	ρ_7	ρ_8	ρ_9	ρ_{10}
2	−1	2	1	−1	0	6	−8	−17	16	0
10	0	0	0	0	0	−1	−9	−18	27	1
20	0	0	1	−2	3	−1	−20	−16	33	1
40	−1	1	−1	−7	−1	−7	−8	−46	10	0
70	3	−2	1	11	−7	16	−54	−98	0	0

Table V.4: Deviation of Bulk vertical density ρ in percentage for grown structures at 1000 K with various incident kinetic energies averaged over 10 independent runs.

E(eV)	ρ_1	ρ_2	ρ_3	ρ_4	ρ_5	ρ_6	ρ_7	ρ_8	ρ_9	ρ_{10}
2	0	0	0	0	0	0	−7	− 22	28	1
10	0	0	0	0	−1	−3	−13	−19	26	1
20	0	0	1	−1	−4	−4	−16	−10	33	0
40	4	1	−5	8	−1	0	−11	−86	0	0
70	6	1	−3	7	15	−6	−78	−98	0	0

Figure V.1: Radial distribution functions g(r) for grown structures at 1 K with various incident kinetic energies averaged over 10 independent runs. Origin of each curve is shifted upwards for clarity.

Figure V.2: Radial distribution functions g(r) for grown structures at 300 K with various incident kinetic energies averaged over 10 independent runs. Origin of each curve is shifted upwards for clarity.
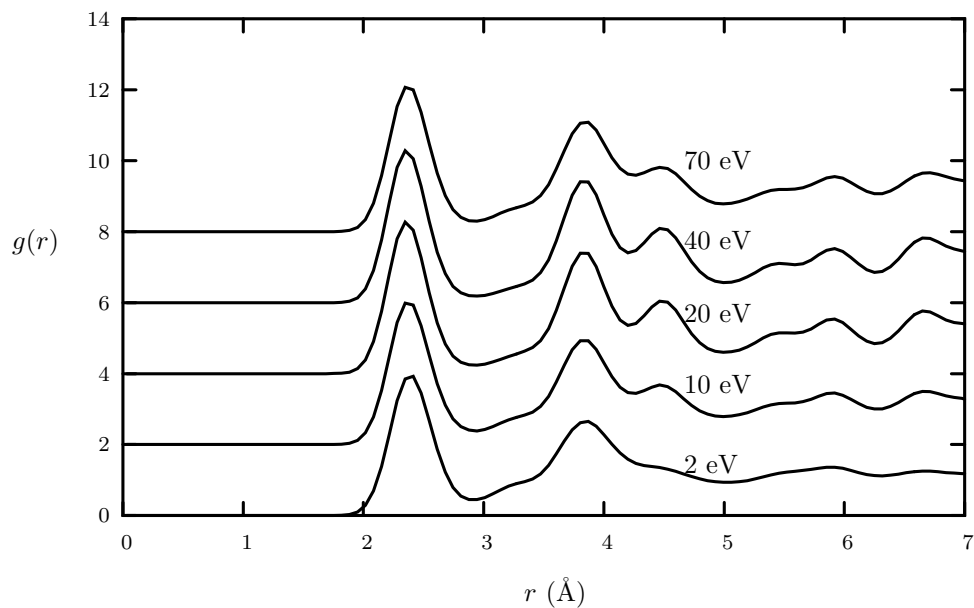
Figure V.3: Radial distribution functions g(r) for grown structures at 1000 K with various incident kinetic energies averaged over 10 independent runs. Origin of each curve is shifted upwards for clarity.
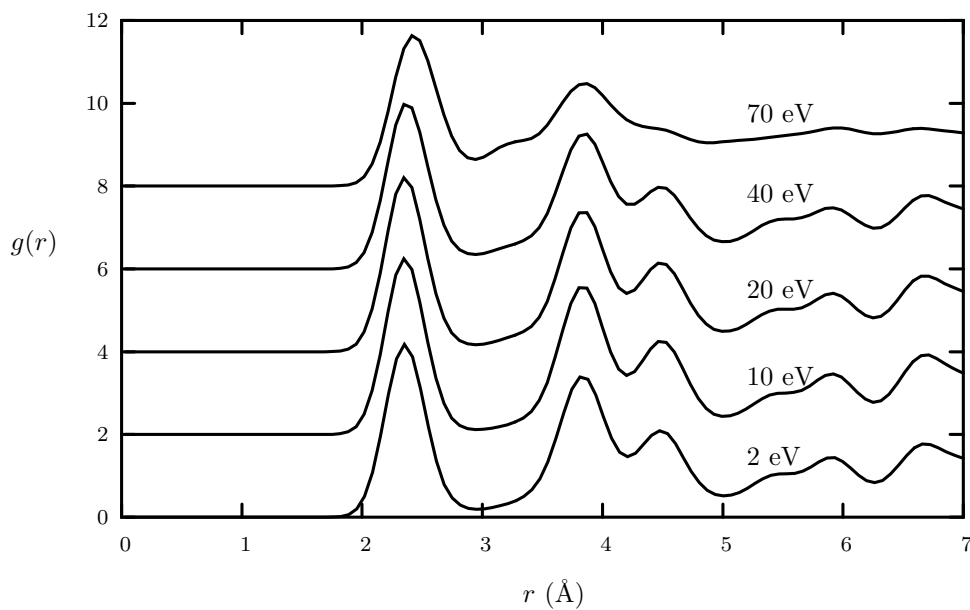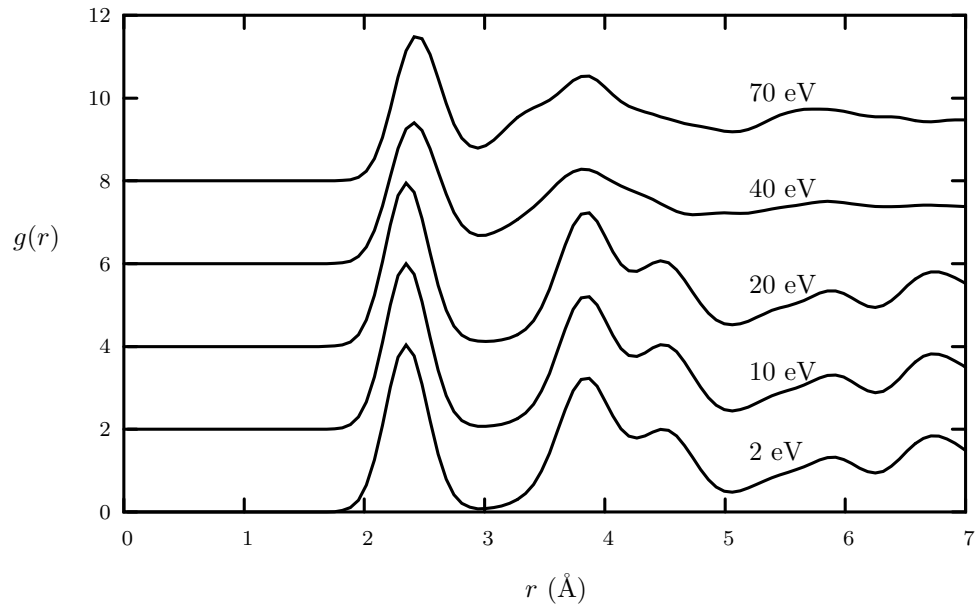
V.4   Radial Distribution Function

In Figure V.1 - V.3 the radial distribution function (RDF) for the grown films are presented. We have found a strong dependence of the radial distribution function on the incident particle energy. At very low temperatures as low as 1 K, we found that it is necessary to increase the incident energy to have a RDF close to that of crystalline sample. We have found that the shoulder of the second peak as well as other higher shell peaks developed more clearly for kinetic energy ≥ 10 eV. As the substrate temperature get increased to room temperature, we found that the radial distribution function resembles to that of crystalline silicon even at low kinetic energy. Increasing the kinetic energy to 20 eV enhances the shape of RDF even more, however, at 40 eV although we still have a crystalline shape

of RDF, it starts to alter slightly towards the amorphous shape. At 70 eV the RDF shape is typically amorphous with no shoulder on the second peak and the peaks corresponding to outer shell atoms disappeared.

For growth at higher temperatures, we do not have very pronounced differences in the behavior of RDF from that of room temperature case, except we found that for the case using kinetic energy $\geq$ 40 eV we get an amorphous-like RDF.

V.5 Coordination Number

In Table V.5 - V.5 we show the coordination number distribution as calculated by integrating up to the first minimum in the radial distribution function. We found that in all grown films the majority of atoms are fourfold coordinated. We have noticed in both simulations that small percentages of atoms are twofold and three-fold coordinated with nearly the same value. We did not find any dependence of the amount of under-coordinated atoms on kinetic energy or substrate temperature, and moreover we found that these unsaturated coordination numbers correspond to atoms which are laying on the surface and in the highest layers. In all simulations we have noticed the existence of very small number of atoms with coordination numbers of six and a little larger percent of atoms with coordination numbers of five. Even though we believe that the existence of over-coordinated atoms might be due to the very short simulation time interval compared to the experimental relaxation times, fivefold coordination is commonly known in silicon clusters [123] and sixfold in liquid silicon [8]. In general, we found that
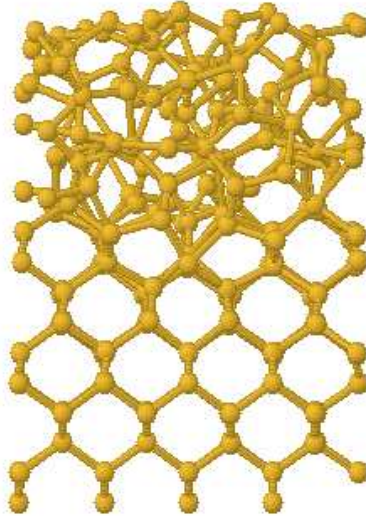
Figure V.4: Snapshot of amorphous structure grown at 1 K. The lowest 9 mono-layers represent the substrate.

the amount of atoms with fourfold and fivefold coordination numbers depends strongly on the substrate temperature and the incident energy. For growth at 1 K and with 2 eV kinetic energy we found 0.24 (24 %) of atoms are fivefold coordinated. Increasing kinetic energy will decrease the percentage of fivefold co-ordinated atoms to the favor of fourfold coordination number. At kinetic energy equal to 40 eV we had the highest amount of fourfold coordinated atoms being equal to 0.73, and with the lowest fivefold coordinated ones of about 0.09 only.

For higher-temperature growth, in general, we found high quality crystalline films characterized by less fivefold coordinated atoms and high amount of four-fold coordinated atoms for using incident energy ≤ 20 eV. As the kinetic energy becomes ≥ 40 eV, we found that the amount of atoms which are fourfold coordi-nated decreased to favor the over-coordinated atoms. We found that crystalline material grown at high temperatures using the window of incident energy ≤ 20
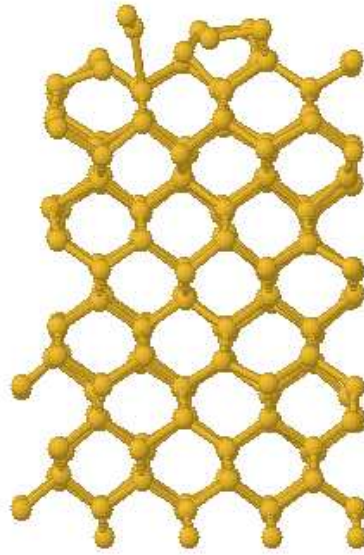
Figure V.5: Snapshot of crystal structure grown at 1000 K. The lowest 9 mono-layers represent the substrate.

eV, is better than any film grown at low temperature.

V.6   Bond Angle Distribution

In the Figure V.6 - V.8, we present the bonding angle distribution for all the grown films. We found a strong dependence of bonding angle distribution on kinetic energy. For all grown films we found the existence of one dominant peak around the tetrahedral angle 109.5° as expected. For the growth at 1 K, the height of peak gets bigger and sharper as the kinetic energy increases, except for the highest energy case of 70 eV.

Different behavior have been noticed for 300 K case, as kinetic energy decreases from 70 to 2 eV the peak gets sharper and higher especially for the 10 eV-case, where we have the sharpest peak. This can be expected since we had the

Table V.5: Coordination number distribution Q_Z in percentage for grown structures at 1 K with various incident kinetic energies averaged over 10 independent runs.

E(ev)	Q_2	Q_3	Q_4	Q_5	Q_6
2	3	11	61	24	1
10	4	13	66	16	1
20	6	14	70	10	0
40	4	14	73	9	0
70	1	10	66	22	1

Table V.6: Coordination number distribution Q_Z in percentage for grown structures at 300 K with various incident kinetic energies averaged over 10 independent runs.

E(eV)	Q_2	Q_3	Q_4	Q_5	Q_6
2	3	11	77	8	0
10	5	11	80	4	0
20	4	13	77	6	0
40	2	17	67	13	1
70	2	10	54	30	3

Table V.7: Coordination number distribution Q_Z in percentage for grown structures at 1000 K with various incident kinetic energies averaged over 10 independent runs.

E(eV)	Q_2	Q_3	Q_4	Q_5	Q_6
2	4	11	82	1	0
10	5	13	80	2	0
20	4	17	77	3	0
40	2	15	55	26	2
70	1	11	48	36	4

best coordination number distribution for that case. For the highest temperature case, we found that peaks can develop as long as kinetic energy ≤ 20 eV.
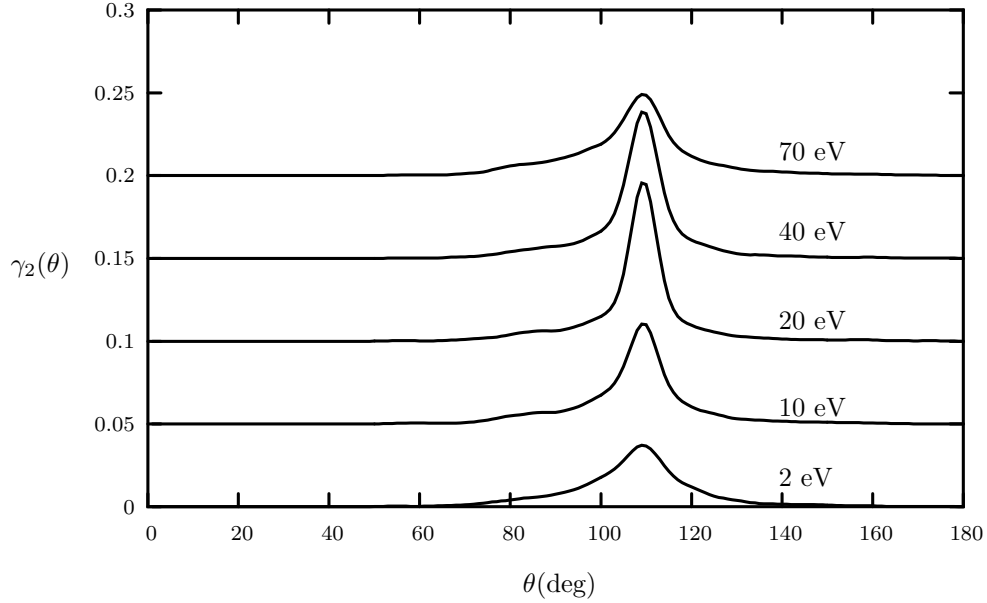

Figure V.6: Bonding angle distribution functions γ_2 for grown structures at 1 K with various incident kinetic energies averaged over 10 independent runs. Origin of each curve is shifted upwards for clarity.

V.7 Dihedral Angle Distribution

The long range ordering of the grown film can be investigated with the use of dihedral angle distribution (DAD). The dihedral angle is defined as follows [124]: Given a chain of three bonds connecting two third neighbors, the two pairs of bonds sharing the common central bond define two intersecting planes. The dihedral angle is the angle between these two planes. It worth to notice here that using this definition the diamond phase exhibits only peaks at angles of $60°$ and $180°$ with a height ratio of 2:1 between these two peaks. Most grown
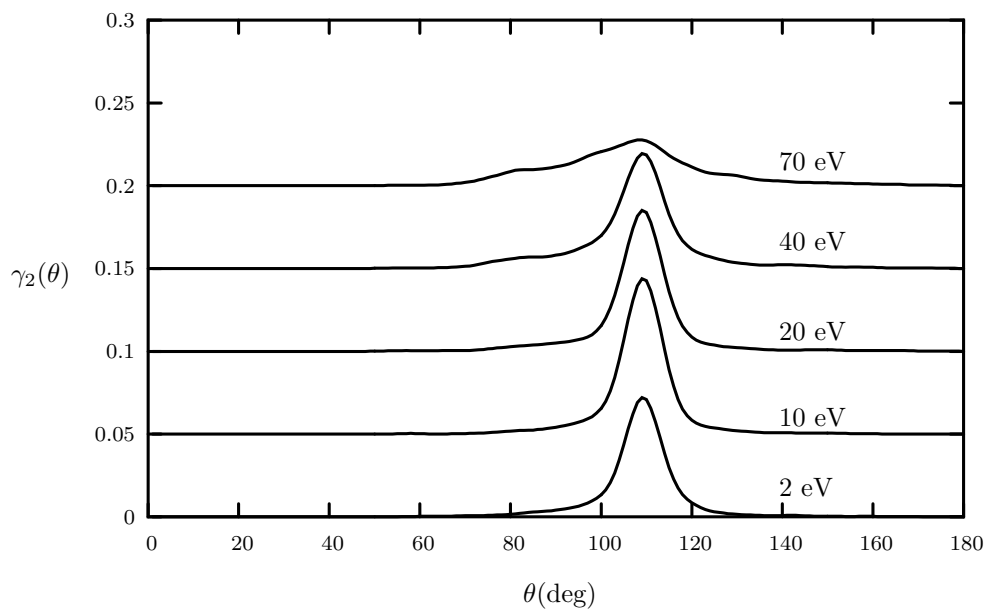
Figure V.7: Bonding angle distribution functions γ_2 for grown structures at 300 K with various incident kinetic energies averaged over 10 independent runs. Origin of each curve is shifted upwards for clarity.

Figure V.8: Bonding angle distribution functions γ_2 for grown structures at 1000 K with various incident kinetic energies averaged over 10 independent runs. Origin of each curve is shifted upwards for clarity.
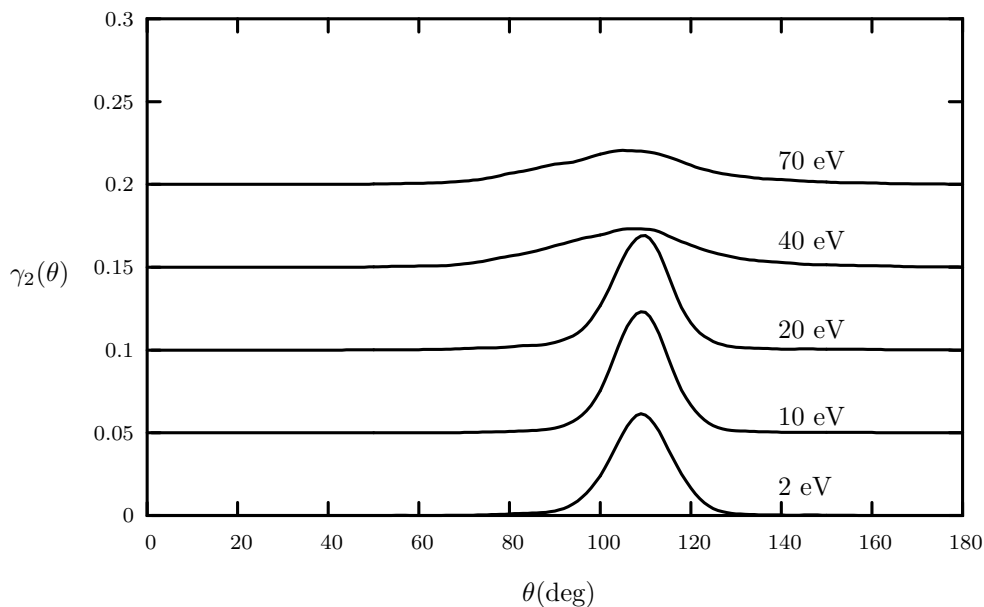
films developed peeks on 60° and 180° as indication of preserved crystallinity. We noticed the dependence of DAD on kinetic energy of incident ions. For films grown at 1 K we found that for the kinetic energy window (10-40 eV), a higher and sharper peaks developed at 60 and 180, increasing kinetic energy beyond 40 leads to broadened peaks with less height. Same behavior was noticed for high temperature growth, namely 300 K, with the exception that the sharpest and highest peaks developed with kinetic energy equal to 10 eV. Films grown at kinetic energy $\geq$ 40 eV and growth temperature of 1000 K did not develop any characteristic peaks in a similar behavior to that of amorphus silicon [124].

Figure V.9: Dihedral angle distribution $\gamma_3(\phi)$ for grown structures at 1 K with various incident kinetic energies averaged over 10 independent runs. Origin of each curve is shifted upwards for clarity.

Figure V.10: Dihedral angle distribution $\gamma_3(\phi)$ for grown structures at 300 K with various incident kinetic energies averaged over 10 independent runs. Origin of each curve is shifted upwards for clarity.
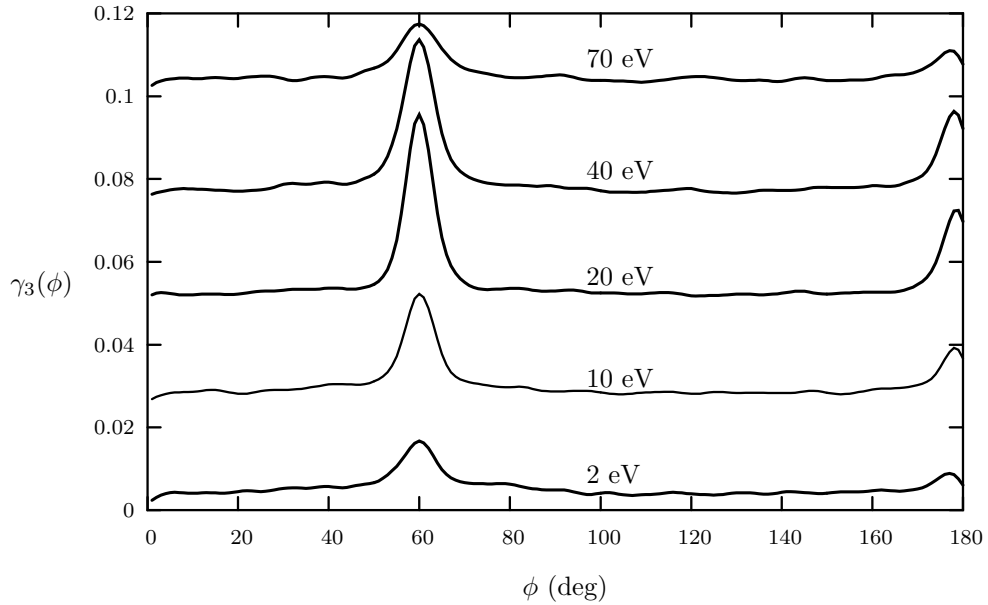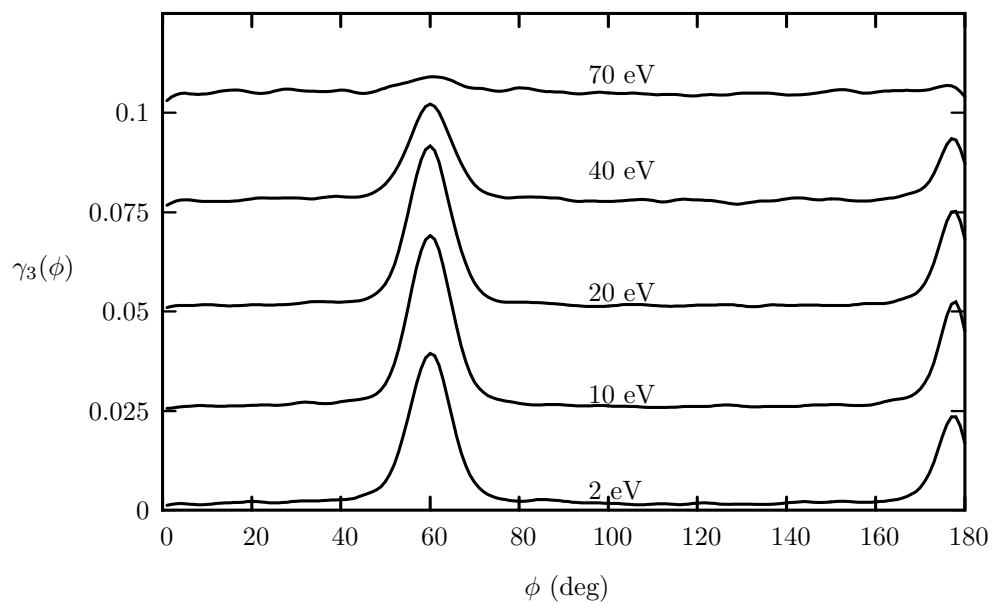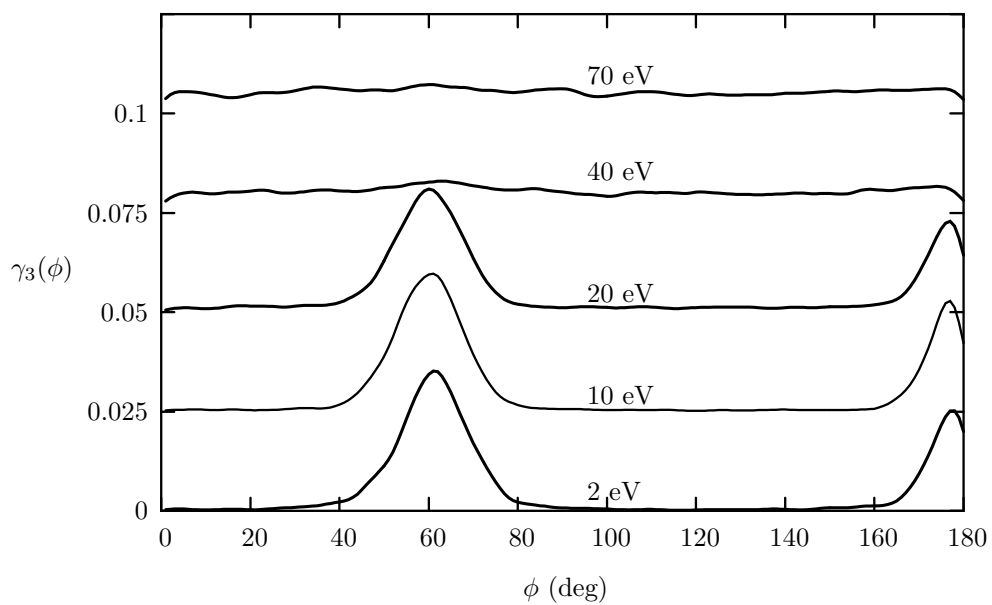

Figure V.11: Dihedral angle distribution $\gamma_3(\phi)$ for grown structures at 1000 K with various incident kinetic energies averaged over 10 independent runs. Origin of each curve is shifted upwards for clarity.

V.8 Discussion

We have performed extensive molecular dynamics simulation of film growth on Si(001) in a manner similar to growth conditions used in the laboratory. The simulation of film growth was achieved as a function of substrate temperature as well as particle incident kinetic energy.

For growth at extremely low temperature, we found that crystalline portion can be enhanced if the the deposited atom have the enough energy to find the epitaxial cite, breaking the dimmer reconstruction turning it from 2×1 to 1×1, which can be implemented by increasing the incident particle energy. on the other hand we found that in general the crystalline films grown at low temperature are not in high quality as those obtained at higher temperature. This result can be in agreement with the experimental result of Rabalias *et al.*[116], who found that, the growth mode, crystalline quality, and number of defects in the films are found to be extremely sensitive to both substrate temperature at low temperature and ion energy at low energy. Our results are in agrement with the theoretical results of Schneider *et al.* [125] results who have found similar results for MD simulation for a similar system Si/Si(111). They have noticed that as substrate temperature increases the grown film goes in transition from amorphous to crystalline structure.

For growth at higher temperatures, we found that crystalline film with high quality can be grown with kinetic energy ≤ 20 eV. Our results for higher temperature growth are in good agreement with other experimental results, especially

with Orrman-Rossiter *et al.* [111, 112] who have shown that the crystalline quality of silicon films get enhanced monotonically as ion energy is decreased from 100 to 10 eV for substrate temperatures $\geq 350°$C, and with Matsuoka and Tohno [113] have shown that crystalline films of silicon can be grown at $320°$C for Si^+ ion energies ≤ 25 eV. We have found that growing at higher incident energy can lead to deformation and defects in the grown films at higher temperature with relative agrement with Matsuoka and Tohno [113] who found that defect density increased drastically for energies above 50 eV.

CHAPTER VI

SUMMARY AND CONCLUSION

Using *ab initio* total energy calculations we have performed detailed investigation of the atomic geometry of clean and Mg adsorbed Si(001) surface for 1/4, 1/2 and full monolayer coverages. We have investigated the adsorption sites, the energetics and the reconstruction of Si(001) surface after Mg adsorption. We have found that our results agree well with the existing experimental observations.

For the 1/4 ML coverage we have found two favorable adsorption sites, namely *c* and *s* with a relative adsorption energy difference of only 0.25 eV per adatom. Our results agree well with the room-temperature results of Hutchison *et al.* [60] and of Cho *et al.* [63]. For the case of half monolayer coverage, our results gave 2×1 reconstruction with the Mg adatoms on *c-c* sites. The high temperature result of Kubo *et al.* [61] for the same coverage suggested that it contains two Mg adatoms located nearly on *c-c* sites but distorted by the existence of an extra Si atom which causes the symmetry to be a 2×2. For the case of full

monolayer coverage, we have found that the adsorption model in which all the Mg atoms occupy all the s sites with 2×1 construction is more favorable than 2×2 reconstruction in which Mg atoms occupy two shallow and two cave sites having an adsorption energy difference of only 0.05 eV per adatom. The next favorable case having 0.07 eV per adatom smaller adsorption energy than the most preferable s-s-s-s case is the p-p-h-h configuration with a 2×1 symmetry, but just slightly away from 1×1 geometry. This may suggest that more than 1 ML coverage might lead to a 1×1 phase consistent with the LEED results of Kim *et al.* [62] who reported that the 1×1 phase corresponds to 2 ML coverage.

The model of adsorption that can be concluded from our theoretical results is that for the low coverage, Mg atoms will be adsorbed mostly on c sites and less likely on s sites, which continues until the coverage reaches to 1/4 ML. As the coverage exceeds 1/4 ML, the Mg atoms are adsorbed on the c-c sites and on the s-s sites along $[\bar{1}10]$ with almost equal probabilities until the surface becomes saturated at 1/2 ML, where it is going to have domains of c-c and s-s phases with 2×1 and 2×2 reconstructions, respectively. Further increase in coverage will result into s-s-s-s, c-c-s-s and even p-p-h-h domains with 2×1, 2×2 and almost 1×1 reconstructions, respectively.

We have used *ab initio* calculations also to present a detailed investigation of the atomic geometry and energetic stability of the Sb-nondiffused, Sb-diffused, and Sb-segregated models for 1 ML coverage of Sb on the Si(001)-(2×1) and Ge(001)-(2×1) surfaces. We have calculated the surface stress for the Si(001) and Ge(001) surfaces capped with a monolayer of any Sb, and its evolution as the

Sb atoms get interdiffused into the substrate. We have found that interdiffusion of Sb into deeper layers will be energetically unfavorable, however, it might still take place due to the considerable relief of the anisotropy in the surface stress. We believe that interdifusion of Sb into Ge(001) as a response to stress relief, followed by diffusion back onto the surface due to an energy-lowering mechanism, will lead to a less ordered Sb/Ge(001) surface.

Finally we have used empirical molecular dynamics methods to study the effect of substrate temperature and energy of incident atoms on the quality of grown thin films. We have found that crystal with high quality can be obtained at room and higher temperatures using kinetic energy particles ≤ 20 eV in agrement with other experimental results. Growth with higher kinetic energy may lead to diffusion of incident atoms into the substrate.

REFERENCES

[1] R. E. Schlier and H. E. Farnsworth, *J. Chem. Phys*. **30**, 917 (1959).

[2] J. A. Appelbaum, G. A. Baraff, and D. R. Hamann, *Phys. Rev. B* **14**; *ibid* 588 (1976); *ibid* **15**, 2408 (1977).

[3] D. J. Chadi, *Phys. Rev. Lett*. **43**, 43 (1979).

[4] R. M. Tromp, R. J. Hamers, and J. E. Demuth, *Phys. Rev. Lett*. **55**, 1303 (1985).

[5] R. J. Hamers, R. M. Tromp, and J. E. Demuth, *Phys. Rev. B* **34**, 5343 (1986).

[6] T. Tabata, T. Aruga, and Y. Murata, *Surf. Sci*. **179**, L63 (1987).

[7] Y. Enta, S. Suzuki, and S. Kono, *Phys. Rev. Lett*. **65**, 2704 (1990).

[8] F. Stillinger and T. Weber, *Phys. Rev. B* **31**, 5262 (1985).

[9] M. Born and J. R. Oppenheimer, *Ann. Physik.* **84**, 457 (1927).

[10] D. R. Hartree, *Proc. Cam. Phil. Soc.* **24**, 89 (1928); *ibid* **24**, 111 (1928); *ibid* **24**, 426 (1928).

[11] W. Pauli, *Z. Physik.* **31**, 765 (1925).

[12] J. C. Slater, *Phys. Rev.* **34**, 1293 (1929); *ibid* **35**, 509 (1930).

[13] V. Fock, *Z. Physik.* **61**, 126 (1930).

[14] L. H. Thomas, *Proc. Camb. Phil. Soc.* **23**, 542 (1927).

[15] E. Fermi, *Rend. Accad. Naz. Lincei* **6**, 602 (1927).

[16] P. Hohenberg and W. Kohn, *Phys. Rev.* **136**, 864 (1964).

[17] W. Kohn and L. J. Sham, *Phys. Rev.* **140**, 1133 (1965).

[18] D. M. Ceperly and B. J. Alder, *Phys. Rev . Lett*. **45**, 566 (1980).

[19] J. P. Perdow and A. Zunger, *Phys. Rev. B* **23**, 5048 (1981).

[20] J. P. Perdew and Y. Wang, *Phys. Rev. B* **45**, 13244 (1992).

[21] J. P. Perdew, K. Burke and M. Ernzerhof, *Phys. Rev. Lett.* **77**, 3865 (1996) and refrence therein.

[22] J. A. Alonso and L. A. Girifalco, *Phys. Rev. B* **17**, 3735 (1978).

[23] J. P. Perdew and M. R. Norman, *Phys. Rev. B* **26**, 5445 (1982).

[24] A. Baldereschi, *Phys. Rev. B* **7**, 5212 (1973).

[25] D. J. Chadi and M. L. Cohen, *Phys. Rev. B* **8**, 5747 (1973).

[26] H. J. Monkhorst and J. D. Pack, *Phys. Rev. B* **13**, 5188 (1976).

[27] J. D. Pack and H. J. Monkhorst, *Phys. Rev. B* **16**, 1748 (1977).

[28] D. J. Chadi, *Phys. Rev. B* **16**, 1746 (1977).

[29] R. A. Evarestov and V. P. Smirnov, *Phys. Stat. Sol. b* **119**, 9 (1983).

[30] S. Froyen, *Phys. Rev. B* **39**, 3168 (1989).

[31] Martin Fuchs and Mathias Scheffler, *Comp. Phys. Commun.* **119**, 67 (1999).

[32] D. D. Koelling and B. N. Harmon, *J. Phys. C***10**, 3107 (1977).

[33] D. R. Hamann, *Phys. Rev. B* **40**, 2980 (1989).

[34] N. Troullier and J. L. Martins, *Phys. Rev. B* **43**, 1993 (1991).

[35] S. G. Louie, S. Froyen, and M. L. Cohen, *Phys. Rev. B* **26**, 1738 (1982).

[36] L. Kleinman and D. M. Bylander, *Phys. Rev. Lett.* **48**, 1425 (1982).

[37] D. Vanderbilt, *Phys. Rev. B* **41**, 7892 (1990).

[38] M. C. Payne, M. P. Teter, D. C. Allan, T. A. Arias, and J. D. Joannopoulos, *Rev. Mod. Phys.* **64**, 1045 (1992).

[39] R. Car and M. Parinello, *Phys. Rev. Lett.* **55** 4894 (1995).

[40] R. P. Feynman, *Phys. Rev.* **56**, 340 (1939).

[41] H. Balmance, T. Halicioglu and W. Tiller, *Phys.Rev. B* **46**, 2250 (1992).

[42] K. Ding and H. C. Anderson, *Phys. Rev. B* **34**, 6987 (1986).

[43] M. Lardaji and D. Landau, *Phys. Rev. B* **51**, 4894 (1995).

[44] B. J. Alder and T. E Wainwright, *J. Chem. Phys.* **27**, 1208 (1957), *ibid* **31**, 459 (1959).

[45] A Rahman, *Phys. Rev. A* **136**, 405 (1964).

[46] F. H. Stillinger and A. Rahman, *J. Chem. Phys.* **60**, 1545 (1974)

[47] D. W. Heerman, "*Computer Simulation Methods in Theoritical Physics*", (Springer-Verlag, Berlin, 1990).

[48] M. P. Allen and D. J. Tildesley, "*Computer Simulation of Liquids*", (Oxford University Press, Oxford, 1987).

[49] C. W. Gear, "*Numerical initial value problems in ordinary diffrential equations*", (Prentice-Hall, Englewood Clifs, NJ, 1971).

[50] L. Verlet, *Phys. Rev.* **159**, 98 (1967).

[51] W. C. Swope, H. C. Anderson, P. H. Berens, and K. R. Wilson, *J. Chem. Phys.* **76**, 637 (1982).

[52] D. Poter, "*Computational physics*", (Willy, New York 1972).

[53] H. C. Anderson, *J. Chem. Phys.* **72**, 2384 (1980).

[54] S. Nos, *Mol. Phys.* **52**, 255 (1984).

[55] W. G. Hoover, *Phys. Rev. A* **31**, 1695 (1985).

[56] M. Parrinello and A. Rahman, *J. Chem. Phys.* **80**, 860 (1984).

[57] Eisaku Miyoshi, Hirotoshi Mori, Shinobu Tanaka, and Yoshiko Sakai, *Surf. Sci.* **5**14, 383 (2002) and references therein.

[58] M. R. J. van Buuren, C. L. Griffiths, and H. van Kempen, *Surf. Sci.* **3**14, 172 (1994).

[59] Y. Kawashima, H. Tanabe, T. Ikeda, H. Itoh, and T. Ichinokawa, *Surf. Sci.* **3**19, 165 (1994).

[60] P. Hutchison, M. M. R. Evans, and J. Nagami, *Surf. Sci.* **4**11, 99 (1998).

[61] Osamu Kubo, Alexander A. Saranin, Andrey V. Zotov, Toru Harada, Tadashi Kobayashi, Nobumitsu Yamaoka, Jeong-Tak Ryu, Mitsuhiro Katayama, and Kenjiro Oura, *Jpn. J. Appl. Phys.* **39**, 3740 (2000).

[62] J. S. Kim, K. W. Ihm, C. C. Hwang, H. S. Kim, Y. K. Kim, C. Y. Park, J. H. Boo, and S. B. Lee, *J. Korean Phys. Soc.* **35**, S550 (1999).

[63] E. S. Cho, C. H. Lee, C. C. Hwang, J. C. Moon, J. h. Oh, K. Ono, M. Oshima, K. S. An, and C. Y. Park, *Surf. Sci.* **523**, 30 (2003).

[64] G. S. Khoo and C. K. Ong, J. Phys.: Condens. Matter **6**, 8141 (1994).

[65] A. Brinkman, D. Mijatovic, G. Rijnders, V. Leca, H. J. H. Smilde, I. Oomen, A. A. Golubov, F. Roesthuis, S. Harkema, H. Hilgenkamp, D. H. A. Blank, and H. Rogalla, *Physica* **C353**, 1 (2001).

[66] A. Plecenik, L. Satrapinsky, P. Kús, S. Gazi, S. Benakca, I. Vávra, and I. Kostic, *Physica C* **363**, 224 (2001).

[67] Jun Wang, J. A. Hallmark, D. S. Marshall, W. J. Ooms, Pablo Ordejón, Javier Junquera, Daniel Sánchez-Portal, Emilio Artacho, and José M. Soler, *Phys. Rev. B* **60**, 4968 (1999).

[68] R. Shaltaf, E. Mete, and Ş. Ellialtıoğlu, *Phys. Rev. B* **69**, 125417 (2004).

[69] X. Gonze, J. M. Beuken, R. Caracas, F. Detraux, M. Fuchs, G.-M. Rignanese, L. Sindic, M. Verstraete, G. Zerah, F. Jollet, M. Torrent, A. Roy, M. Mikami, Ph. Ghosez, J.-Y. Raty, D.C. Allan, *Comp. Matter. Sci.* **25** (2002) 478.

[70] The ABINIT code is a common project of the Université Catholique de Louvain, Corning Incorporated, and other contributors *(URL http://www.abinit.org)*.

[71] M. Levinstein, *Handbook Series on Semiconductor Parameters*, Vol. **1,2** (World Scientific, London, 1999).

[72] R. W. G. Wyckoff, "*Crystal Structures*", Vol. 1, 2nd ed., (Interscience, New York, 1963) pp. 241–243.

[73] C. M. Wei, H. Huang, S. Y. Tong, G. S. Glander and M. B. Webb, *Phys. Rev. B* **42**, 11284 (1990).

[74] P. S. Mangat, P. Soukiassian, K. M. Schirm, Z. Hurych, L. Spiess, S. P. Tang, A. J. Freeman, and B. Delley, *Phys. Rev. B* **47**, 16311 (1993).

[75] D. F. Shanno, *J. Optim. Theo. Appl.* **46**, 87 (1985).

[76] G. X. Qian, R. M. Martin, and D. J. Chadi, *Phys. Rev. B* **38**, 7649 (1988).

[77] M. A. Boshart, A. A. Bailes, III and L. E. Seiberling. *Phys. Rev. Lett*. **77**, 1087 (1996).

[78] G. Li and Y. C. Chang. *Phys. Rev. B* **50**, 8675 (1994).

[79] P. Krüger and J. Pollmann. *Phys. Rev. B* **38**, 10578 (1988); *ibid Phys. Rev. B* **47**, 1898 (1993).

[80] M. Richter, J. C. Woicik, J. Nogami, P. Pianetta, K. E. Miyano, A. A. Baski, T. Kendelewicz, C. E. Bouldin, W. E. Spicer, C. F. Quate, and I. Lindau, *Phys. Rev. Lett.* **65**, 3417 (1990).

[81] J. Nogami, A. A. Baski, and C. F. Quate, *Appl. Phys. Lett.* **58**, 475 (1991).

[82] Y. J. Lee, J. W. Kim and S. Kim. *J. Phys.: Cond. Matter* **9**, L583, (1997).

[83] O. Alerhand, J. Wang, J. Joannopoulos, E. Kaxiras and R. Becker. *Phys. Rev. B* **44**, 6534 (1991).

[84] R. Tromp, A. Denier and M. Reuter. *Phys. Rev. Lett.* **68**, 2313 (1992).

[85] A. A. Saranin, A. V. Zotov, V. G. Kotlyar, V. G. Lifshits, O. Kubo, T. Harada, T. Kobayashi, N. Yamaoka and K. Oura. *Phys. Rev. B* **65**, 033312 (2001).

[86] L. H. Chan, E. I. Altman, L. E. Seiberling, *Phys. Rev. Lett.* **77**, 1087 (1996).

[87] D. Vanderbilt, *Phys. Rev. Lett.* **59** 1456 (1987).

[88] G. P. Francis and M. C. Payne, *J. Phys. Cond. Matter* **2**, 4395 (1990).

[89] A. Ramstad, G. Brocks, and P. J. Kelly, *Phys. Rev. B* **51**, 14504 (1995).

[90] M. Richter, J. C. Woicik, J. Nogami, P. Pianetta, K. E. Miyano, A. A. Baski, T. Kendelewicz, C. E. Bouldin, W. E. Spicer, C. F. Quate, and I. Lindau, *Phys. Rev. Lett. 65*, 3417 (1990).

[91] S. Tang and A. Freeman. Phys. Rev. B 47, 1460 (1993).

[92] J. H. Cho and M. Kang. Phys. Rev. B 51, 5080 (1995).

[93] J. G. Che, K. M. Zhang and X. D. Xie, *Phys. Rev. B* **60**, 4784 (1999).

[94] A. Garcia and J. Northrup, *Phys. Rev. B* **48**, 17350 (1993).

[95] R. D. Meade and D. Vanderbilt, "*Proceedings of the 20th International Conference on Physics of Semiconductors*", edited by E. M. Anastassakis and J. D. Joannapoulos (World Scientific, Singapore, 1990)

[96] S. Jenkins and G.P. Srivastava. *Surf. Sci.* **352**, 411 (1996).

[97] M. M. Bülbül, M. Çakmak, G. P. Srivastava, and K. Çolakoğlu, *Phys. Rev. B* **64**, 155318 (2001).

[98] J. H. Cho, M. H. Kang, *Phys. Rev. B* **61**, 1688 (2000).

[99] Yao He, X. H. Zhang, J. G. Che, *Phys. Rev. B* **66**, 193304 (2002).

[100] M. Lohmeier, H. A. van der Vegt, R. G. van der Silfhout, E. Vlieg, J. M. C. Thornton, L. E. Macdonald, P. M. L. O. Scholte,

[101] N. Takeuchi, *Phys. Rev. B* **55** 2417 (1997).

[102] S. Jenkins, G. P. Srivastava, *Phys. Rev. B* **56**, 9221 (1997). *Surf. Sci.* **275**, 190 (1992).

[103] M. Çakmak, R. Shaltaf, G.P. Srivastava, and Ş. Ellialtıoğlu, *Surf. Sci.* **532-535** (2003) 661.

[104] R. Shaltaf, M. Çakmak, E. Mete, G.P. Srivastava, and Ş. Ellialtıoğlu, *Surf. Sci.*, in press.

[105] J. A. Venables, G. D. T. Spiller and M. Hanbucken, *Rep. Prog. Phys.* **47**, 399 1984.

[106] R. A. Zuhr, S. J. Pennycook, T. S. Noggle, N. Herbots, T. E. Haynes and B. R. Appleton, *Nucl. Inst. and Meth.* **B37/38**, 16 (1989).

[107] D. G. Armour, *Nucl. Inst. and Meth. B* **89**, 325 (1994).

[108] K. Miyaki and T. Tokuyama, *Thin Solid Films*, **92**, 123(1982).

[109] P. C. Zalm and L. J. Beckers, *App. Phys. Lett.* **41**, 167 (1982).

[110] N. Herbots, B. R. Appleton, T. S. Noggle, R. A. Zuhr, and S. J. Pennyocook, *Nucl. Inst. and Meth. B* **13**, 250 (1986).

[111] K. J. Orrman-Rossiter, A. H. Al-Bayati, D. G. Armour, S. E. Donnely, and J. A. van den Berg, *Nucl. Inst. and Meth. B* **59/60**, 197 (1991).

[112] K. G. Orrman-Rossiter, D. R. G. Mitchell, S. E. Donnelly, C. J. Rossouw, S. R. Glanvill, P. R. Miller, A. H. Al-Bayati, J. A. van den Berg and D. G. Armour, *Philos. Mag. Lett.* **61**, 311 (1990).

[113] M. Matsuoka and S. Tohno, *J. Vac. Sci. Technol. A* **13**, 305 (1995)

[114] A. H. Al-Bayati, K. J. Boyd, D. Marton, S. S. Todorov, J. W. Rabalias, Z. H. Zhang and W. K. Chu, *J. Appl. Phys.* **76**, 4383 (1994).

[115] A. H. Al-Bayati, S. S. Todorov, K. J. Boyd, D. Marton and J. W. Rabalais, *J. Vac. Sci. Technol. B* **13**, 1639 (1995).

[116] J. W. Rabalais, A. H. AlBayati, K. J. Boyd, and D. Marton, *Phys. Rev. B.* **53**, 10781 (1996).

[117] T. Ohmi, T. Ichikawa, T. Shibata, K. Matsudo and H. Iwabuchi, *Appl. Phys. Lett.* **53**, 45 (1988).

[118] G. K. Wehner, R. M. Warner, Jr., P. D. Wang and Y. H. Kim, *J. Appl. Phys.* **64**, 6754 (1988).

[119] B. Strickland and C. Roland, *Phys. Rev. B* **51**, 5061 (1995).

[120] H. Hensel and M. Herbert Urbassek, *Phys. Rev. B* **58**, 2050 (1998).

[121] H. P. Kaukonen and R. M. Nieminen, *Phys. Rev. Lett.* **68**, 620 (1992).

[122] Hartmut Hensel and Herbert M. Urbassek, *Phys. Rev. B* **58**, 2050 (1998).

[123] Th. Frauenheim, F. Weich, Th. Kohler, S. Uhlmann, D. Porezag, and G. Seifert, *Phys. Rev. B* **52**, 11492 (1995).

[124] I. Tich, R. Car, and M. Parrinello, *Phys. Rev. B* **44**, 11092 (1991).

[125] M. Schneider, I. K. Schuller, and A. Rahman, *Phys. Rev. B* **36**, 1340 (1987).

VITA

Riad Shaltaf was born in Amman in 1973 where he got his primary education. In June 1995 he got his B.Sc. degree in Physics from Yarmouk University in Jordan. In October 1996 he enroled in Middle East Technical University in the Department of Physics where he received his M.Sc. degree in Atomic and Molecular Physics in October 1998. He was accepted to Ph.D. program in the same institute in February 1999. He has worked as a high school teacher for four years. He has been employed as a part-time research assistant in METU since 1999.

Parts of this thesis appear in the following articles :

- "Mg adsorption on Si(001) surface from first principles",

  R. Shaltaf, E. Mete, and Ş. Ellialtıoğlu, *Phys. Rev. B* **69**. 125417, (2004).

- "Ab initio study of the one-monolayer Sb/Ge(001) interface"

  R. Shaltaf, M. Cakmak, E. Mete, G. P. Srivastava, and Ş. Ellialtıoğlu,

  Surf. Sci. in press.

- "Ab initio study of the one-monolayer Sb/Si(001) interface",

  M. Cakmak, R. Shaltaf, G. P. Srivastava, and Ş. Ellialtıoğlu,

  Surf. Sci. **532-535**, 661 (2003).

Other puplished articles

- "Electronic and Structural Properties of a 4d-Perovskite:

  Cubic Phase of SrZrO$_3$",

  E. Mete, R. Shaltaf, and Ş. Ellialtıoğlu, *Phys. Rev. B* **68**, 035119, (2003).

- "Computer simulation of small copper clusters",

  Ş. Erkoc and R. Shaltaf, *Phys. Rev. A* **60**, 3053 (1999).